

REPORT DOCUMENTATION PAGE				Form Approved OMB No. 0704-0188	
<p>The public reporting burden for this collection of information is estimated to average 1 hour per response, including the time for reviewing instructions, searching existing data sources, gathering and maintaining the data needed, and completing and reviewing the collection of information. Send comments regarding this burden estimate or any other aspect of this collection of information, including suggestions for reducing the burden, to Department of Defense, Washington Headquarters Services, Directorate for Information Operations and Reports (0704-0188), 1215 Jefferson Davis Highway, Suite 1204, Arlington, VA 22202-4302. Respondents should be aware that notwithstanding any other provision of law, no person shall be subject to any penalty for failing to comply with a collection of information if it does not display a currently valid OMB control number.</p> <p><b>PLEASE DO NOT RETURN YOUR FORM TO THE ABOVE ADDRESS.</b></p>					
1. REPORT DATE (DD-MM-YYYY) 13-05-2011		2. REPORT TYPE		3. DATES COVERED (From - To)	
4. TITLE AND SUBTITLE Search for the Exotic Wobbling Mode in rhenium-171				5a. CONTRACT NUMBER	
				5b. GRANT NUMBER	
				5c. PROGRAM ELEMENT NUMBER	
6. AUTHOR(S) Pedicini, Eowyn Elise				5d. PROJECT NUMBER	
				5e. TASK NUMBER	
				5f. WORK UNIT NUMBER	
7. PERFORMING ORGANIZATION NAME(S) AND ADDRESS(ES)				8. PERFORMING ORGANIZATION REPORT NUMBER	
9. SPONSORING/MONITORING AGENCY NAME(S) AND ADDRESS(ES) U.S. Naval Academy Annapolis, MD 21402				10. SPONSOR/MONITOR'S ACRONYM(S)	
				11. SPONSOR/MONITOR'S REPORT NUMBER(S) Trident Scholar Report no. 400 (2011)	
12. DISTRIBUTION/AVAILABILITY STATEMENT This document has been approved for public release; its distribution is UNLIMITED					
13. SUPPLEMENTARY NOTES					
14. ABSTRACT The observation of a wobbling band, associated with the $i13/2$ band is a strong indication that a nucleus possesses asymmetric deformation. In order to determine the role of the atomic number on the observation of asymmetric deformation, an experiment was conducted to search for the wobbling mode in $171\text{Re}$ . High-spin states in $171\text{Re}$ were produced in a reaction at Argonne National Laboratory. Reaction gamma rays were detected using germanium detectors in the Argonne Gammasphere spectrometer. These gamma-ray data were subsequently analyzed at the Naval Academy. Seven decay sequences in $171\text{Re}$ were established, but the focus of this project was based on sequences feeding into the previously determined $i13/2$ band. Two bands were found to feed into the $i13/2$ structure, and their characteristics have been assessed to determine if these sequences are associated with wobbling.					
15. SUBJECT TERMS wobbling, $171\text{Re}$ , Gammasphere					
16. SECURITY CLASSIFICATION OF:			17. LIMITATION OF ABSTRACT	18. NUMBER OF PAGES 66	19a. NAME OF RESPONSIBLE PERSON
a. REPORT	b. ABSTRACT	c. THIS PAGE			19b. TELEPHONE NUMBER (Include area code)

U.S.N.A. --- Trident Scholar project report; no. 400 (2011)

**SEARCH FOR THE EXOTIC WOBBLING MODE IN  $^{171}\text{Re}$**

by

Midshipman 1/C Eowyn E. Pedicini  
United States Naval Academy  
Annapolis, Maryland

---

(signature)

Certification of Advisers Approval

Associate Professor Daryl J. Hartley  
Physics Department

---

(signature)

---

(date)

LT Brian J. Cummings, USN  
Chemistry Department

---

(signature)

---

(date)

Acceptance for the Trident Scholar Committee

Professor Carl E. Wick  
Associate Director of Midshipman Research

---

(signature)

---

(date)

## Abstract

It is often assumed that the nucleus of an atom is spherical; however, this is not always the case. At excited or high-spin states, where the nucleus is rotating very rapidly, it can either stretch or compress along a body-fixed, principal axis, giving it the shape of an American football or a doorknob. Very rarely, a nucleus can assume an asymmetric shape where it does not rotate around a principal axis but instead wobbles. This wobbling motion is analogous to the spinning motion of an asymmetric top. The wobbling mode has been found in several isotopes of lutetium (Lu). Surprisingly, this mode was not observed in the neighboring hafnium (Hf) and thulium (Tm) isotopes and was only recently found in an isotope of tantalum (Ta).

The observation of a wobbling band, associated with the  $i_{13/2}$  band is a strong indication that a nucleus possesses asymmetric deformation. In order to determine the role of the atomic number on the observation of asymmetric deformation, an experiment was conducted to search for the wobbling mode in  $^{171}\text{Re}$ . High-spin states in  $^{171}\text{Re}$  were produced in a reaction at Argonne National Laboratory. The off-center collisions between the  $^{55}\text{Mn}$  beam and the  $^{120}\text{Sn}$  target nuclei resulted in large amounts of angular momentum (spin) in the new compound nucleus. To dispel this angular momentum,  $\gamma$  rays were emitted by the nucleus; these  $\gamma$  rays were detected using germanium detectors in the Gammasphere spectrometer at Argonne National Laboratory.

These  $\gamma$ -ray data were subsequently analyzed at the Naval Academy.  $\gamma$  rays that were emitted in coincidence, or nearly simultaneously, came from one unpaired nucleon in its decay to the ground state. Seven decay sequences in  $^{171}\text{Re}$  were established, but the focus of this project was based on sequences feeding into the previously determined  $i_{13/2}$  band. Two bands were

found to feed into the  $i_{13/2}$  structure, and their characteristics have been assessed to determine if these sequences are associated with wobbling.

Keywords: wobbling,  $^{171}\text{Re}$ , Gammasphere

## Acknowledgments

To begin with, I must extend my deepest gratitude and love to my family: my parents and my brother. Without their support and encouragement, I would not have made it to the Naval Academy, much less through it. To my parents, thank you for teaching me not to be afraid to ask questions and for instilling in me the willpower to find the answers. I developed a love of science because of you. To Colin, thank you for always being better than me at math so I had something to work towards.

I also wish to thank my advisers, Dr. Daryl Hartley and LT Brian Cummings. Professor Hartley, thank you for agreeing to advise a chemist and thank you for your patience as I learned, forgot, and relearned most everything. Despite appearances, I really did learn some computer programming. I also learned a lot about nuclear physics from you and a little about baseball and politics. You truly have been a mentor to me these past couple years, and I look forward to many more such conversations in the future. LT Cummings, thank you for agreeing to be one of my advisers within a couple months of arriving at the Academy. I also enjoyed our submarine talks and the Chemistry open house nights.

A special thanks to the Chemistry Department for allowing me to do research with the Physics Department, and to the Physics Department for accepting me.

To my roommates, thank you for putting up with all the late nights I spent studying and for forcing me to relax when I got so wound up in academics. Finally, to all of 17<sup>th</sup> Company, thank you for humoring me and listening to all my science jokes. As much as we all look forward to graduation, I'll miss living with you and look forward to future reunions.

**Table of Contents**

<b>Abstract</b>	<b>1</b>
<b>Acknowledgments</b>	<b>3</b>
<b>1. Introduction</b>	<b>5</b>
<b>2. Experimental Details and Data Preparation</b>	<b>7</b>
A. Heavy Ion Reaction	7
B. Gammasphere	10
C. Experimental Details	12
D. Data Preparation	14
<b>3. Data Analysis and Theory</b>	<b>21</b>
A. Data Analysis	21
B. Angular Correlation Ratios	24
C. Shell Model and Deformed Shell Model	26
D. Cranked Shell Model	32
E. Bands	33
<b>4. Configurations</b>	<b>42</b>
<b>5. Wobbling</b>	<b>53</b>
<b>6. Conclusions and Future Work</b>	<b>58</b>
<b>7. Bibliography</b>	<b>59</b>
<b>8. Appendices</b>	<b>61</b>
Appendix 1: Definition of Terms	61
Appendix 2: Angular Correlation Ratios	63

## 1. Introduction

The universe tends towards symmetry, whether it is the radial symmetry of a snowflake or a spiral galaxy, or the bilateral symmetry of the human body. Even structures such as the atomic nucleus often exhibit symmetry. However, deviations from symmetry attract attention and make for interesting studies to understand the cause of the asymmetry. Of over 3000 atomic nuclei, only five have been found to exhibit an asymmetric (or triaxial) shape. Most of these nuclei have a proton number  $Z=71$  and a neutron number near  $N=94$ . The goal of this study is to determine the range of the region these triaxial shapes occur by investigating the nuclear structure of  $^{171}\text{Re}$ , with  $Z=75$  and  $N=96$ .

The way that asymmetry is observed in a nucleus is to rotate the nucleus, which excites the nucleus into higher energy states. As the nucleus returns to its lowest energy state, it dissipates energy by emitting specific sequences of  $\gamma$  rays called bands. If the nucleus is in fact asymmetric, it will exhibit a wobbling motion, much like that of an asymmetric top when it spins. This exotic wobbling motion will create a distinct decay sequence that can be observed through the use of a  $\gamma$ -ray coincidence experiment.

A wobbling band was first discovered in  $^{163}\text{Lu}$  [ØDE 01] and later discovered in  $^{161, 165, 167}\text{Lu}$  [BRI 06, SCH 03, AMR 03]. This indicated that asymmetric nuclei might be a characteristic of the  $Z$  (proton)  $\sim 72$ ,  $N$  (neutron)  $\sim 94$  region [SCH 03]. Nuclei in the region of 94 neutrons, a magic number for triaxial, strongly deformed (TSD) structures, were expected to show evidence of wobbling. However, no evidence of wobbling was found in nearby Ta, Hf, or Tm [HAR 05a, HAR 06, HAR 05b, PAT 07], even though  $^{163}\text{Tm}$  ( $N=94$ ) contained several TSD structures [PAT 07]. This led to the theory that wobbling was unique to the Lu isotopic chain.

However,  $^{167}\text{Ta}$ , with  $N=94$ , was recently found to exhibit wobbling characteristics [HAR 09] which now has the nuclear structure community wondering how prevalent these asymmetric shapes are in this region. The experiment conducted in March 2010 focused on two nuclei: the  $N=94$  isotone  $^{169}\text{Re}$  was studied to determine if it, too, exhibits the wobbling mode [HAR 10], and  $^{171}\text{Re}$  was also studied because a previous experiment conducted by Ref. [CAR 93] showed there were transitions that were indicative of the possibility of wobbling.

The paper will begin with an introduction into the experimental method used to produce the excited states, including a description of how and where the experiment was carried out. Then there will be a discussion on the various data preparation tasks that were required before the data could be analyzed. This is followed by the data analysis section, which includes a brief history of several shell models used to describe the atomic nucleus. An outline of the decay sequences that are observed comes after that, followed by a description of how band configurations were assigned. Finally, there is a discussion on the potential for wobbling in  $^{171}\text{Re}$  and a summary of future work that can be conducted.



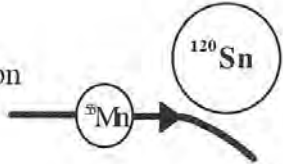

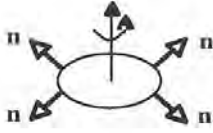
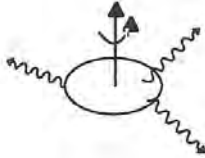
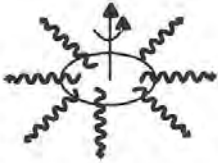

## 2. Experimental Details and Data Preparation

### A. Heavy Ion Reaction

In order to study the high-spin, excited states mentioned above, large amounts of angular momentum must be imparted to the nucleus. This is analogous to spinning a top and then observing it slow down. Unlike an ordinary top that constantly dissipates energy, a quantum top such as a nucleus gives off energy in discrete packets, which are  $\gamma$  rays. One method of spinning nuclei is through the heavy-ion fusion-evaporation reaction. In this method, a beam of light nuclei is aimed at a target of heavier nuclei. The energy of the beam must be great enough to overcome the repulsion that will occur when the two positively charged nuclei come close. For this experiment, the ATLAS accelerator at Argonne National Laboratory was used to create the beam of  $^{55}\text{Mn}$  nuclei.

The off-center collisions between the beam and target nuclei will produce a compound nucleus of high excitation energy and spin. Figure 2.1 depicts the de-excitation process after fusion has occurred. The nucleus will first diffuse some energy through particle emission. While there is a possibility for both proton and neutron emission, neutron emission is more likely because the neutron is uncharged. Protons are less likely to be emitted because they must penetrate the Coulomb barrier resulting from their positive charge. Particle emission is capable of removing large amounts of energy but removes very little angular momentum. As seen in Figure 2.1, following particle emission, the nucleus undergoes a period where it emits statistical, or random  $\gamma$  rays, but once again, very little angular momentum is removed. The nucleus is so excited that the density of energy states is too great for individual  $\gamma$ -ray sequences to be identified. These become background  $\gamma$  rays that are not of interest. Finally, after about  $10^{-12}$

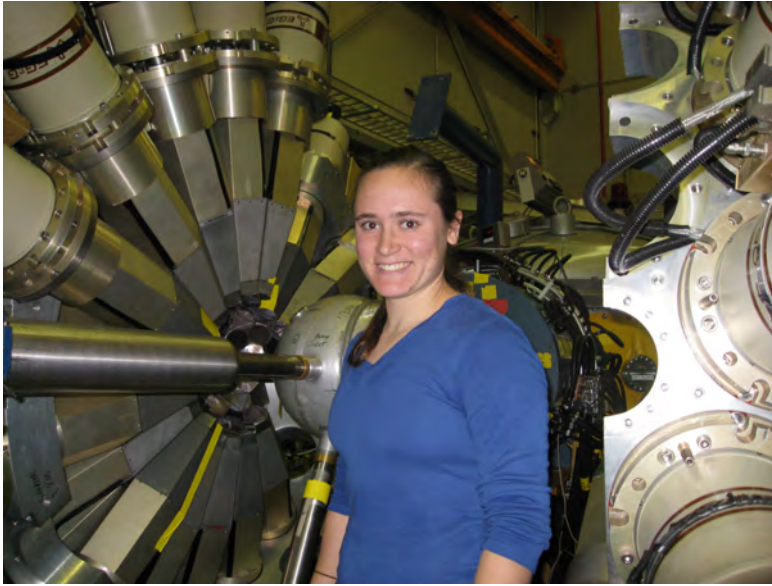
seconds, the nucleus is cool enough to emit discrete sequences of  $\gamma$  rays, known as rotational bands. At this point, the density of states has decreased, so individual transitions can be detected. It is this final process that allows for the structure of the nucleus to be studied through an analysis of the rotational bands. The entire process only takes about a nanosecond ( $10^{-9}$  seconds), but the shape of the nucleus can be inferred from these decay sequences.

		Time Scale (sec)	Rotational Frequency (MeV)	Number of Rotations
Preformation		$<0$		0
Formation of Compound Nucleus		$10^{-22}$	.50 $\sim 1 \times 10^{20}$ Hz	$<1$
Particle Emission (Neutrons)		$10^{-19}$	.50	10-100
Statistical Cooling (Gammas)		$10^{-17}$ - $10^{-12}$	.50	$10^3$ - $10^8$
Quadrupole Emission (Gammas)		$10^{-12}$ - $10^{-10}$	.50-0	$10^8$ - $10^{10}$
Ground State		$10^{-9}$	0	$10^{11}$

**Figure 2.1: Heavy ion reaction pathway, showing the formation of the compound nucleus and the subsequent dissipation of energy to reach the ground state.**

## B. Gammasphere

In order to detect the decay sequences, or rotational bands, an array of many  $\gamma$ -ray detectors surrounding the target is needed. For this reason, the experiment was conducted at Argonne National Laboratory using an instrument called Gammasphere [JAN 96], which can be seen in Figure 2.2, where the target was placed inside the spherical shell in the center of the picture. The metal rod extending to the left side of the picture is where the beam travels after being accelerated. Gammasphere can have as many as 110 germanium (Ge) detectors, with bismuth germanate ( $\text{Bi}_4\text{Ge}_3\text{O}_{12}$ , or BGO) shields surrounding the Ge detectors to reject  $\gamma$  rays scattered out of the Ge detectors and reduce the background noise (see description below). Gammasphere is the world's largest  $\gamma$ -ray detector array. Detectors are placed at the following angles (assuming forward-backward symmetry): 10 detectors are at  $17.3^\circ$ , 10 are at  $31.7^\circ$ , 10 are at  $37.4^\circ$ , 20 are at  $50.1^\circ$ , 10 are at  $58.3^\circ$ , 20 are at  $69.8^\circ$ , 10 are at  $79.2^\circ$ , 10 are at  $80.7^\circ$ , and 10 are at  $90^\circ$ . The system is controlled by a remote computer, and data are written to a USB hard drive. The decay sequences mentioned above release all of their  $\gamma$  rays within a nanosecond (ns). Data will be recorded when multiple detectors observe  $\gamma$  rays within a 120 ns coincident window. These coincident events contain information about the detector that fired (and thus at what angle the  $\gamma$  ray was emitted) and the energy of the  $\gamma$  rays. This information was “unpacked” into a coincidence matrix for analysis as described below.



**Figure 2.2: Gammasphere.** The target ( $^{120}\text{Sn}$ ) went into the ball in the center of the picture. The beam ( $^{55}\text{Mn}$ ) came through the rod on the left side of the picture.

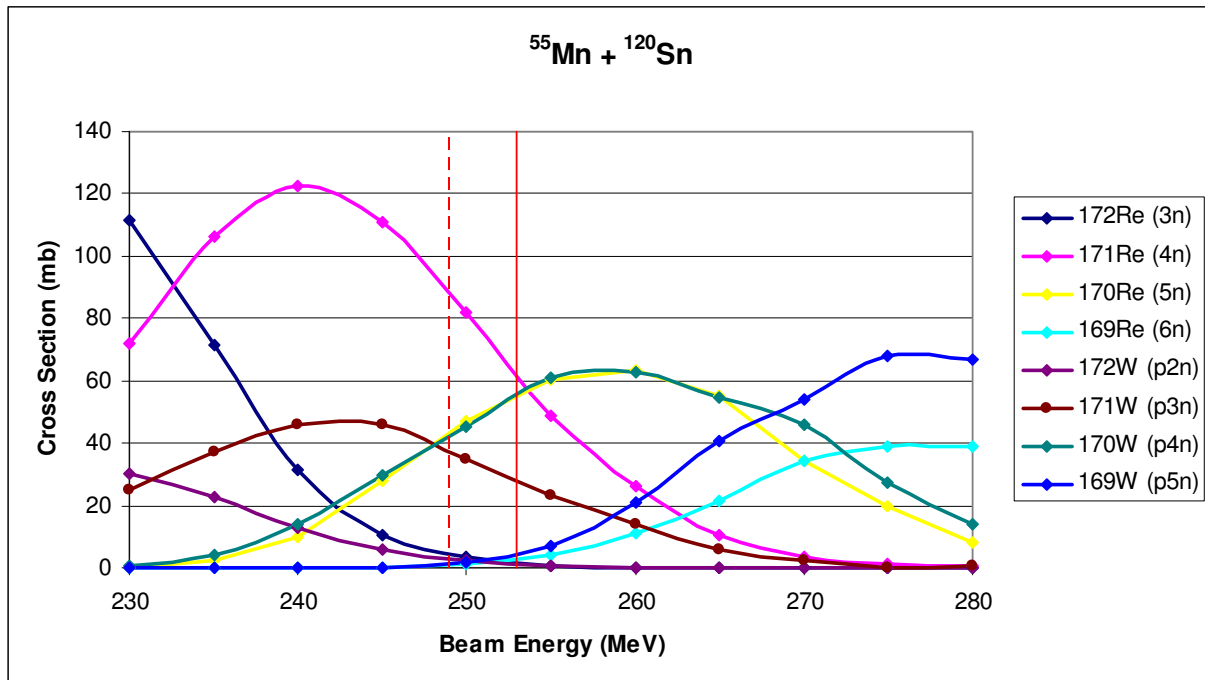
The goal of the detectors is to capture as many of the actual  $\gamma$  rays created by the reaction as possible. High purity Ge detectors are used to absorb the  $\gamma$  rays released by the reaction. When a  $\gamma$  ray collides with the Ge crystal in the detector and is completely absorbed, many electrons are freed in the crystal. If this happens, a total charge proportional to the energy of the  $\gamma$  ray can be measured at a central contact in the detector. This is stored as a channel number, which is linearly correlated with  $\gamma$ -ray energy. However, this method is most dominant for lower-energy photons. Another effect called Compton scattering also occurs, where the incident  $\gamma$  ray scatters off an electron in the detector. The electron only absorbs a fraction of the energy of the incident photon; if the remaining energy of the photon is absorbed by other electrons, the detected energy will still be the same as if all the energy had been absorbed by a single electron. A problem occurs when the scattered  $\gamma$  ray exits the detector before all its energy has been absorbed; this will result in false energy observations and will increase the unwanted

background. One solution for this problem is to surround the germanium detector with another detector made of bismuth germanate, or BGO. Any time the BGO detects a  $\gamma$  ray that has been scattered out of the germanium detector, it electronically vetoes the simultaneous event (of the Compton scattered  $\gamma$  ray) in the germanium detector. This greatly reduces the background signal and allows for the observations of weaker signals that are often most physically interesting.

### C. Experimental Details

The experiment for this project occurred in March 2010. In this reaction,  $^{171}\text{Re}$  was formed through the  $^{120}\text{Sn}(^{55}\text{Mn}, 4n)$  reaction. This means a high-energy beam of  $^{55}\text{Mn}$  struck a target of  $^{120}\text{Sn}$  and formed a compound nucleus of  $^{175}\text{Re}$ . In order to dissipate energy, the nucleus first underwent particle emission and emitted four neutrons, leaving  $^{171}\text{Re}$ . However, other nuclei are expected to form as well, resulting from the emission of three or five neutrons, as well as channels that emit a proton with varying numbers of neutrons. Projected Angular momentum Coupled Evaporation (PACE) calculations were used to predict the cross sections and angular momenta for given reactions at varying energies. A cross section is related to the probability of a particular nucleus to be made. As can be seen in Figure 2.3, the 4n channel will dominate at lower energies (240 MeV), but at higher beam energies, other channels will be more prominent because more particles are likely to be emitted from the nucleus. However, higher beam energies are desired to impart more angular momentum into the compound nucleus. The goal of the PACE calculations is to determine a beam energy that balances a good cross section with a large amount of spin. The actual beam energy for the experiment was set at 253 MeV.

Although PACE calculations are useful for predicting beam energies, they tend to run about 5 MeV high compared to actual observations. This is because the calculations assume an infinitely thin target. During the experiment, when the beam strikes the target, the nuclei will slow down a little, thus losing energy. At 253 MeV, the 4n channel (which produces  $^{171}\text{Re}$ ), the p4n channel (which produces  $^{170}\text{W}$ ), and the 5n channel (which produces  $^{170}\text{Re}$ ), were expected to be produced at nearly identical rates, as can be seen by the solid red line. The dotted red line shows the actual cross sections produced. The  $\gamma$ -decay sequences of  $^{170}\text{W}$  [REC 85],  $^{171}\text{W}$  [ESP 94],  $^{172}\text{W}$  [ESP 94], and  $^{170}\text{Re}$  [WAN 04] are well known and were used to discriminate between those decay sequences and the new sequences of  $^{171}\text{Re}$ .

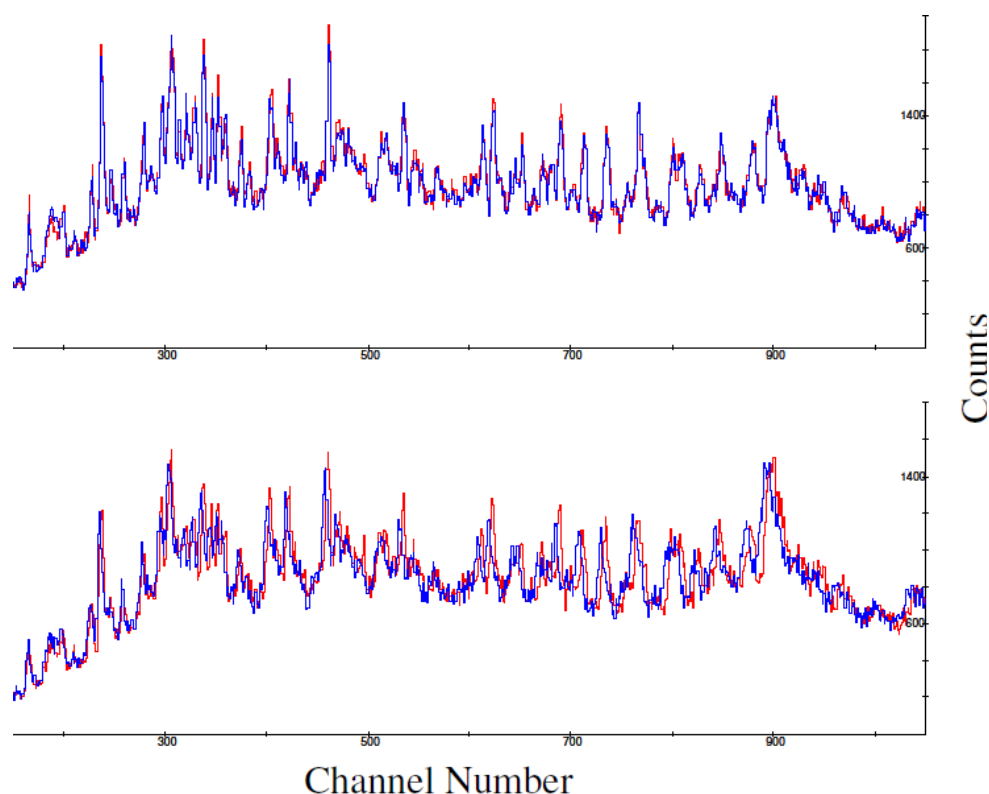


**Figure 2.3:** PACE calculations for the  $^{55}\text{Mn} + ^{120}\text{Sn}$  reaction. The solid red line indicates the beam energy based on PACE calculations, while the dotted line represents the actual cross sections produced.

## D. Data Preparation

Before the data from the detector can be analyzed, it must be checked for accuracy and consistency. First, the detectors must be checked against each other to ensure that  $\gamma$  rays of the same energy are being read into the same channel number. The data were divided into sixteen runs, each totaling about an hour of time. Using the first run as the reference, each subsequent run was compared to the initial run. A spectrum of counts versus channel number was plotted for 100 detectors in each run. Ideally, throughout the experiment, each detector will remain consistent, where the  $\gamma$ -ray peaks line up in the same channel number. However, this was not always the case. Detector 46 underwent what is called a gain shift and began recording data into lower channels. This can be seen in Figure 2.4, which is a plot that compares detectors 44 and 46, that are in the same ring of Gammasphere and thus should have identical Doppler shifts (explained below) from the initial run. The upper plot shows data recorded from detector 44; the red shows data recorded in the first hour while the blue plot is data from a run eleven hours later. In the bottom plot, which shows data collected by detector 46, the same color scheme was used, and the gain shift can clearly be seen as the data from the first hour is recorded into higher channel numbers than the data from the run in the eleventh hour.



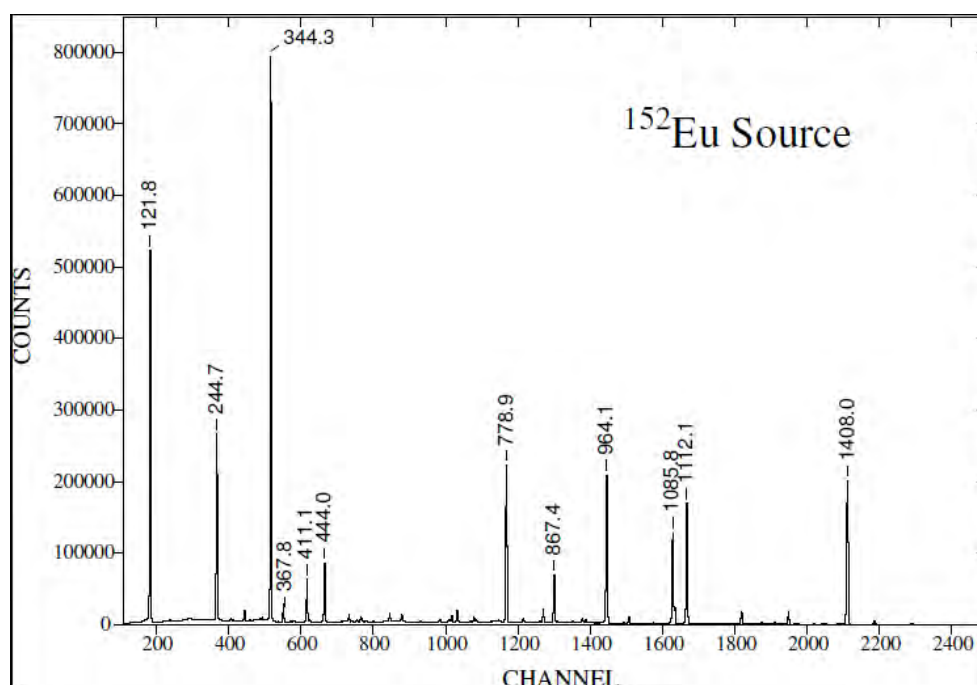


**Figure 2.4: Data from the first hour (red) and eleventh hour (blue). The top spectra shows data from detector 44 (no gain shift) while the bottom spectra shows the gain shift in detector 46.**

Once a gain shift was recognized, a correlation factor needed to be determined to correct the gain shifts. To do this, specific  $\gamma$  ray energies were compared from detector 46 and from detector 44, which is in the same ring. Because these two detectors are at the same angle, they should record  $\gamma$  rays into the same channel numbers. A plot in Excel was made, using data from detector 44 on the x axis and data from detector 46 plotted on the y axis. The slope and intercept were determined, and this correction factor was applied to detector 46 such that the peaks in the latter runs matched up with those found in earlier runs.

Energy calibrations were performed to convert channel numbers into  $\gamma$ -ray energies. The data from the detectors are stored in channels, which have a linear correlation with the  $\gamma$ -ray

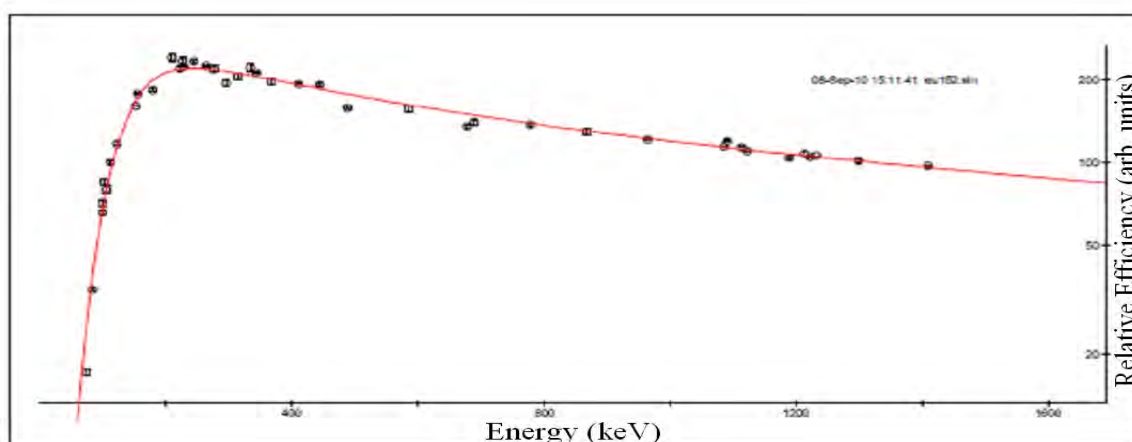
energy. In order to convert channel numbers into  $\gamma$ -ray energies, radioactive sources with known  $\gamma$ -ray energies are used:  $^{243}\text{Am}$ , which has low-energy  $\gamma$  rays,  $^{152}\text{Eu}$ , which emits  $\gamma$  rays across a broad range of energies, and  $^{182}\text{Tl}$ , which emits both low- and high-energy  $\gamma$  rays. These sources have well-known  $\gamma$ -ray energies. Figure 2.5 shows the spectrum for  $^{152}\text{Eu}$ . By plotting  $\gamma$ -ray energy versus channel number, an equation which relates the channel number to the correct  $\gamma$ -ray energy was formulated.



**Figure 2.5: Counts versus channel number for  $^{152}\text{Eu}$ . The x-axis is channel number, while the numbers listed above the peaks are the energies of the  $\gamma$  rays, measured in keV.**

These sources were also used to make an efficiency curve for the detectors. The intensities of the peaks from the sources were compared to known absolute intensities of the sources. For each source, the ratio of the measured intensity to the absolute intensity was taken. This is the relative efficiency. The ratios were then normalized to achieve a smooth curve, which was then used to fit an equation to the data such that the relative efficiency could be determined

for any  $\gamma$ -ray energy. The efficiency curve can be seen in Figure 2.6, which shows that the efficiency for the detectors is not the same for all energies of  $\gamma$  rays. Low energy  $\gamma$  rays have slower collection times, and it is harder to see them before another  $\gamma$  ray enters the detector, leading to less efficiency at the low-energy end. Efficiency tails off at higher energies because higher energy  $\gamma$  rays are more likely to be Compton scattered. As previously discussed, if some of the energy scatters out of the detector and the BGO shielding detects an event, it will veto the event for the detector. The line displays the equation that was fit to the data.



**Figure 2.6: A plot of relative intensity versus channel number, showing the detector efficiency at different energies.**

Finally, the velocity of the compound nucleus needed to be determined. Because the compound nucleus exits the target and is moving forward after it is formed, a Doppler effect, similar to hearing a horn on a moving train, affects the  $\gamma$ -ray energies.  $\gamma$  rays are photons whose energy is  $E_\gamma = hf$ , where  $h$  is Planck's constant and  $f$  is the frequency, analogous to the frequency of a sound wave. If the source of the frequency (*i.e.* the nucleus or the train) is moving, the frequency that is detected will be shifted either higher or lower depending on the angle of the

receiver (i.e. the  $\gamma$ -ray detectors or our ears) to the source. Detectors in front of the nucleus will measure higher energy  $\gamma$  rays than detectors that are behind the nucleus. This can be seen in Figure 2.7. A plot of counts versus channel number was compared for detectors at angles of  $31.7^\circ$ ,  $69.8^\circ$ ,  $90^\circ$ ,  $110.2^\circ$ , and  $148.3^\circ$ . This encompasses two forward detectors, colored blue, which were reading  $\gamma$  rays into higher channel numbers, two rear detectors, shown in red, which were reading  $\gamma$  rays into lower channel numbers, and detectors perpendicular to the direction the compound nuclei will move in, which measures the true energy of the  $\gamma$  rays.

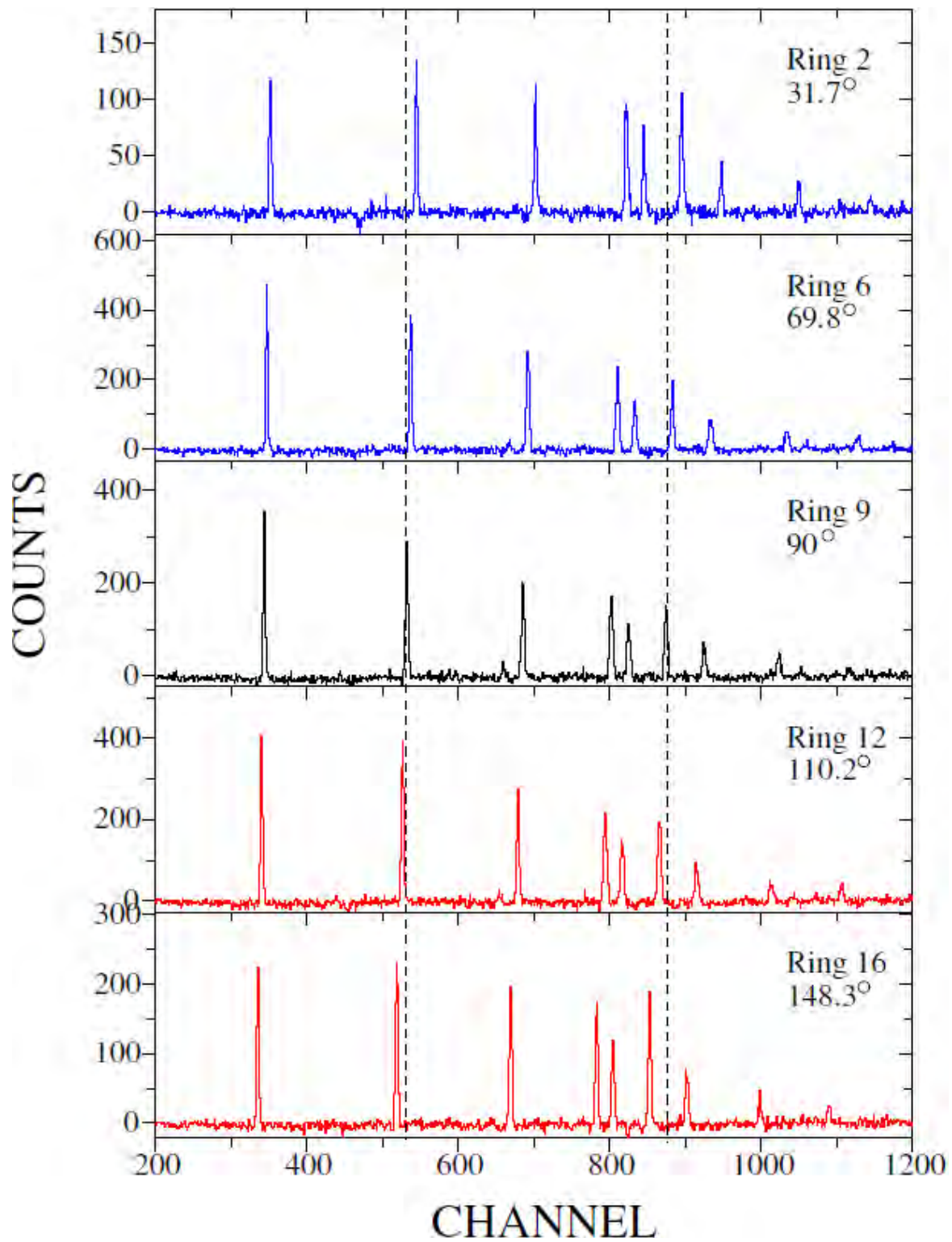
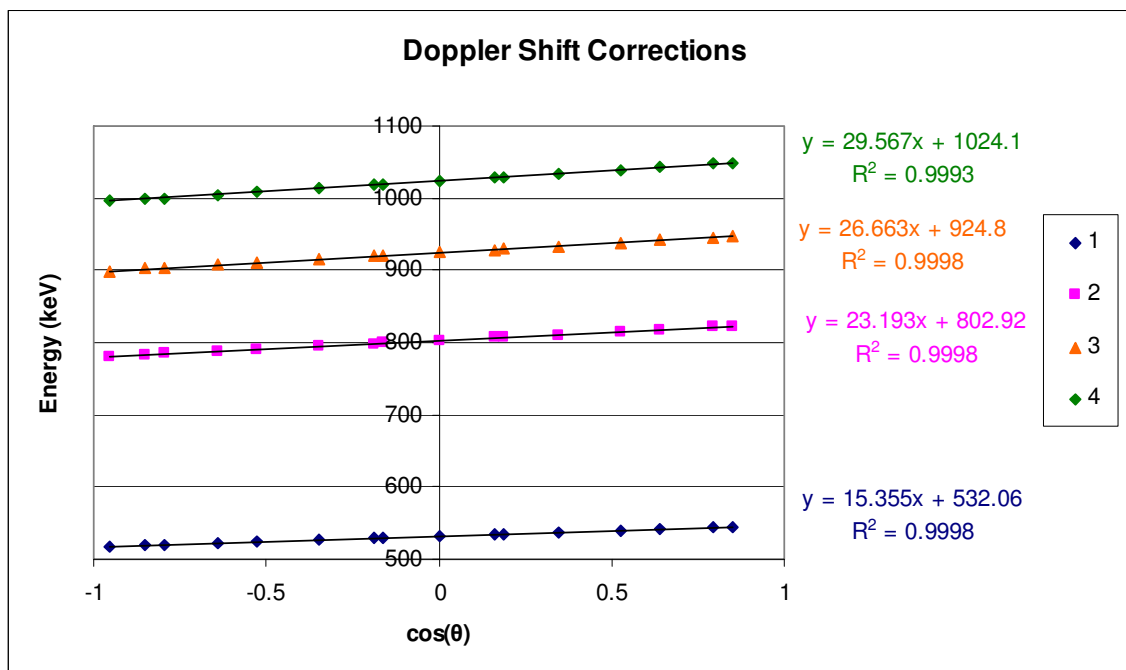


Figure 2.7: The Doppler effect, comparing forward and rear detectors with detectors perpendicular to the source. All spectra shown were from the same gate.

As previously discussed, the detectors are arranged in rings, with each ring at a specific angle to the target. All detectors in a specific ring should read the same energy. The energies of four  $\gamma$  rays were measured in each ring, and this was plotted versus the cosine of the angle of the detectors. As can be seen in Figure 2.8, the measured energy is linearly dependent on the cosine of the detector angle. Using the equation  $E = E_0(1 + \beta \cos \theta)$ , where  $E$  is the measured energy,  $E_0$  is the true energy of the  $\gamma$  ray (determined from the detectors at  $90^\circ$ , where  $\cos \theta = 0$ ), and  $\beta$  is  $v/c$ , where  $v$  is the speed of the nucleus and  $c$  is the speed of light, the detected energy was plotted for detectors at various angles. The speed of the nucleus was determined to be  $0.0289c$ .



**Figure 2.8:** The Doppler effect can be seen in the linear relationship between measured energy and the cosine of the detector angle.

### 3. Data Analysis and Theory

#### A. Data Analysis

Once the data were prepared, they were sorted into a database by a program called Blue [CRO 01]. The sorting was based on coincident events, *i.e.* events in which multiple detectors measured  $\gamma$  rays within a 120 ns window. An event in which three detectors fired within the coincidence window is called a 3-fold event; this naming scheme is used all the way up to 15-fold events. Using Blue, all 3-fold events were sorted into one file. After that, 4-fold events were sorted into another file, and so on, up to 15-fold events. Once this was completed, the data stored in Blue could be used to build coincidence matrices in order to construct the level scheme of  $^{171}\text{Re}$ . The level scheme is made up of different decay sequences; each of these decay sequences is constructed from specific sequences of  $\gamma$  rays.

Figure 3.1a shows a spectrum of all the  $\gamma$  rays that were collected in the experiment. Clearly, there are too many peaks, corresponding to different  $\gamma$ -ray energies, to discern any useful information. If one were to look at one specific  $\gamma$  ray and determine which other  $\gamma$  rays were coincident with it, a two-dimensional matrix ( $E_\gamma \times E_\gamma$ ) would be built. This is analogous to plotting the gating  $\gamma$  ray along the x-axis and all coincident  $\gamma$  rays would be plotted along the y-axis. Figure 3.1b shows a single gate taken on a 457-keV  $\gamma$  ray, which is similar to using a  $E_\gamma \times E_\gamma$  matrix, as it shows all the  $\gamma$  rays coincident with the 457-keV transition. This spectrum has fewer peaks than Figure 3.1a, and these peaks also better define where a sequence (229, 255, 457, *etc.*) can be observed; however, even this spectrum has many peaks resulting from other decay sequences such that it is difficult to construct a band structure. Due to the vast number of  $\gamma$  rays collected, well into the billions, this method is not selective enough. It should be noted

that there are fewer counts per  $\gamma$ -ray energy in Figure 3.1b compared with Figure 3.1a, due to the selectivity, and this is a natural consequence of gating.

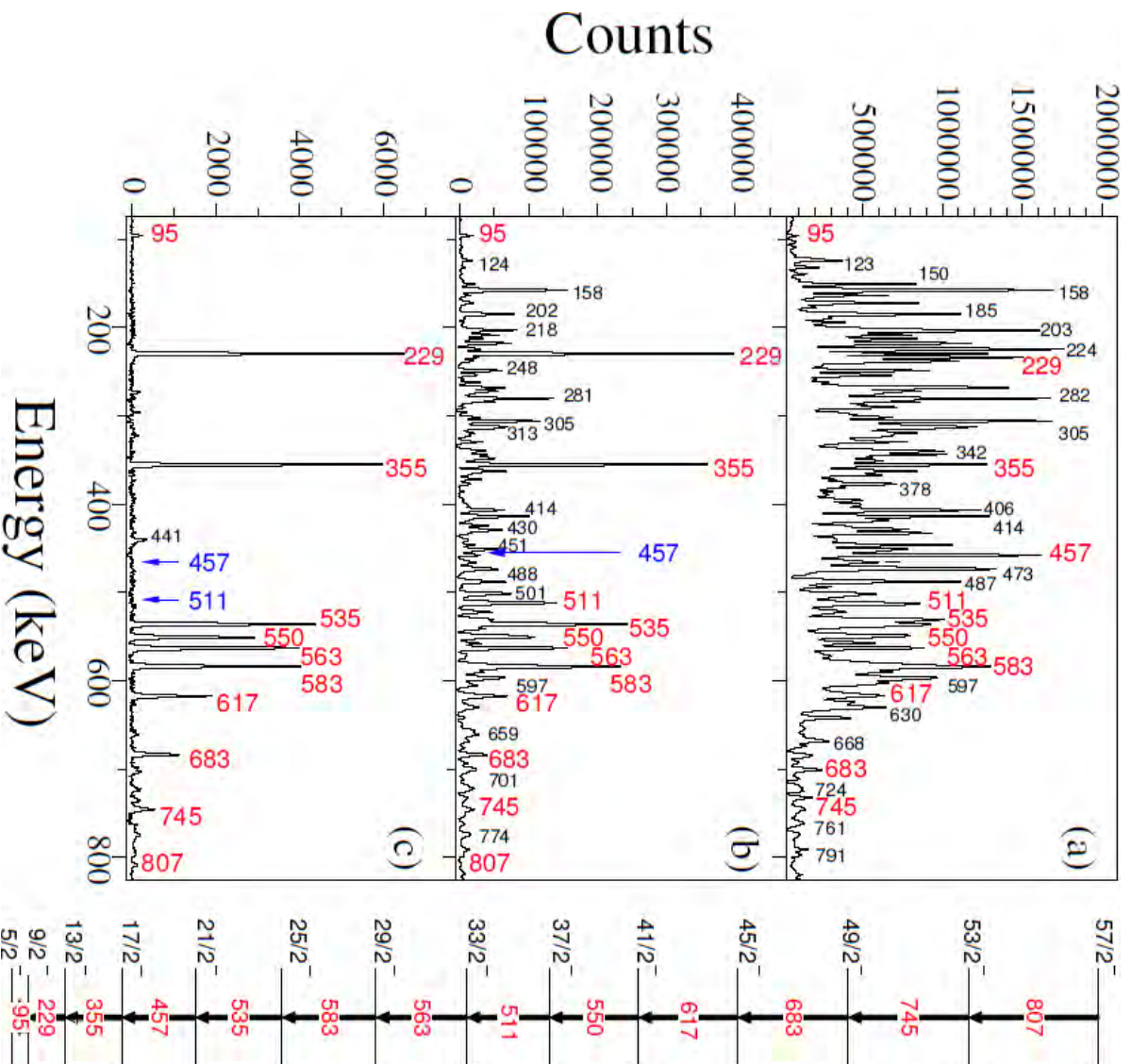


Figure 3.1: a) The entire spectrum of  $\gamma$  rays observed in the experiment. b) A spectrum showing the effect of gating on just the 457 keV  $\gamma$  ray. c) A spectrum showing the effect requiring the 457 and 511 keV  $\gamma$  rays to both be in an event. On the right is the sequence that was constructed from this gating procedure.



Instead of relying on gating on a single  $\gamma$  ray and only looking at those coincident  $\gamma$  rays, a gate could be taken on two  $\gamma$  rays at once. This requires a three-dimensional cube ( $E_\gamma \times E_\gamma \times E_\gamma$ ), which can be imagined as one gating  $\gamma$  ray energy plotted along the x-axis and the other gating  $\gamma$  ray plotted along the y-axis. Any  $\gamma$  rays coincident with both selected  $\gamma$  rays in the same event will be projected on the third axis, or the z-axis. Any  $\gamma$  rays that were not coincident with both of the gating  $\gamma$  rays from the same event are ignored until another gate is taken. There are now fewer peaks from which to determine a single decay sequence as seen in Figure 3.1c, which used gates on the 457 and 511 keV  $\gamma$  rays. The decay sequence, which is shown along the right panel of Figure 3.1, can now be easily discerned; this decay sequence is also listed as Band 1 in Figure 3.8. Most of the peaks in the band could be seen in Figure 3.1a and Figure 3.1b, highlighted in red, but there were too many other  $\gamma$  rays in the spectrum to be able to confidently construct the band. There are still some additional peaks in the double-gated spectrum of Figure 3.1c that are not in the band, but due to the selectivity, it is highly likely that these peaks are associated with this band in some way. Additional gates were then taken to determine how these transitions related to the band, and these transitions were often found to be links to other bands. Once again, the counts per  $\gamma$ -ray energy are again diminished from the single gate. This is a necessary tradeoff: obtaining a cleaner spectrum increases the certainty with which a decay sequence can be determined, but the decrease in counts makes it harder to see weaker transitions.

It is not enough to simply determine which transitions are in a band. As a nucleus decays to its ground state, it emits  $\gamma$  rays in a specific sequence, and this sequence must also be determined. When gates are taken low in a band, the intensity of the gating transitions limits the intensities of the transitions below the gates. It is useful to draw an analogy to a series of

buckets, where water is passed from one bucket to another. When a gate is taken, the intensity of the gating  $\gamma$  rays equates to an amount of water in a bucket. No more water can be added to the buckets (or states) below the gate; if there are other transitions feeding into the band below the gating transitions, they will not be seen. The intensity of the  $\gamma$  rays below the gating  $\gamma$  rays will be approximately equal to the intensity of the gating  $\gamma$  ray. The  $\gamma$  rays above the gating transitions will decrease in intensity as the levels progress toward higher energies. Recall from an earlier section that the nucleus, when it is first created in the reaction, is in a state where the density of states is too high to gather much data. As the nucleus cools, it feeds into discrete sequences, but it can feed these sequences at different energy levels. The same bucket-of-water analogy can be applied here. The highest level in the discrete sequence, when it decays, gives all its intensity (water) to the next lowest level (bucket), but more intensity (water) can be added to that level from the fusion reaction. Each lower level will have greater intensity than the level above it. The  $\gamma$  rays will be ordered based on their intensities with less intense  $\gamma$  rays placed higher in the band.

## **B. Angular Correlation Ratios**

It is also not enough to simply construct the level scheme of  $\gamma$ -ray transitions; the spins of the states must be determined.  $\gamma$  rays are electromagnetic radiation, and in level schemes, the most common transitions are of magnetic dipole (M1), electric dipole (E1), or electric quadrupole (E2) character. Magnetic dipole transitions have a change in spin of one and no

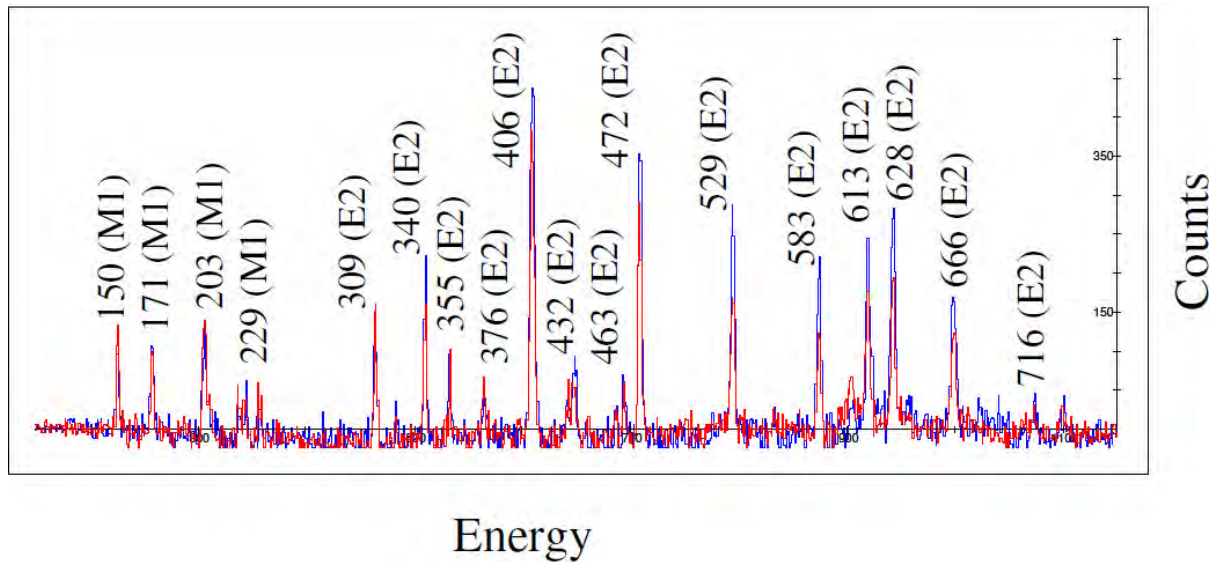
change of parity.\* Electric dipole transitions also have a change of spin equal to one, but they have a change in parity. Electric quadrupole transitions, which can be seen in Figure 3.1 are the most common transitions in rotational nuclei; they have a change in spin of two and no change in parity.

Based on the shape of each radiation pattern (dumbbell shaped for dipole transitions and four-leaf clover for quadrupoles), the type of transition can be determined by comparing the intensity of a  $\gamma$ -ray transition from a perpendicular detector (at  $90^\circ$ ) to the intensity of that same transition from either a forward or a backward detector. Detectors at angles of  $79.2^\circ$  through  $100.8^\circ$  were used for perpendicular measurements, and detectors at angles of  $121.7^\circ$  through  $162.7^\circ$  were used for non-perpendicular measurements. The ratio of the intensities of the  $\gamma$  rays in the backward detectors to the intensities of the  $\gamma$  rays in the perpendicular detectors was calculated. These spectra were obtained from the gating in the Blue database, and the ratios are called angular correlation ratios. Before these measurements were taken on  $^{171}\text{Re}$ , the angular correlation ratios were measured on other nuclei produced in the experiment, specifically  $^{170}, ^{172}\text{W}$  [REC 85, ESP 94]. The character of the  $\gamma$ -ray transitions of these nuclei are well known and served as a benchmark for our ratios. Based on these measurements, E2 transitions produced a ratio of about 1.5, and dipole transitions produced a ratio of about 1. Figure 3.2 shows the angular correlation spectra for one band. The blue spectrum is from the backward detectors while the red spectrum is from detectors perpendicular to the target. When the red and the blue spectra are the same height and overlap, this corresponds to an angular correlation of one, which

---

\* Parity refers to the wavefunction of a particle. A particle is said to have positive parity if changing the position vector of a wavefunction from positive to negative reproduces the wavefunction, while negative parity means that when the position vector of a wavefunction changes from positive to negative, the wavefunction changes sign.

is a dipole transition. When the blue spectrum is greater than the red, this generally corresponds to a ratio of about 1.5 meaning the transition is a quadrupole transition. This technique cannot distinguish between M1 and E1 transitions, which, in this nucleus, are most of the lower energy transitions, but a clear difference in  $\gamma$ -ray intensity can be seen for the higher energy  $\gamma$  rays, which are E2 in character. These figures could then be applied to the ratios found in  $^{171}\text{Re}$ . A full listing of angular correlation ratios and transition type can be found in Appendix 2.



**Figure 3.2: Angular correlation ratios for Band 3. The lower energy  $\gamma$  rays are M1 transitions while the higher transitions are E2.**

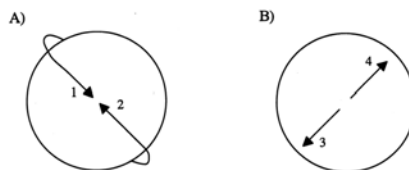
### C. Shell Model and Deformed Shell Model

Before an in-depth discussion on band assignments can be made, a basic introduction to nuclear structure must be given. Although the field of nuclear physics lacks a model that describes the characteristics of all nuclei, the standard starting model of the atomic nucleus is the shell model. This is analogous to the model used to describe electrons in their orbit around the

nucleus. Nucleons, either protons or neutrons, occupy quantized energy levels that can be described by a principle quantum number,  $n$ , the orbital angular momentum quantum number,  $l$ , and the spin quantum number,  $s$ . Just as elements with filled shells of electrons are more stable and less reactive, so too are there magic numbers of nucleons. Nuclei containing a magic number (2, 8, 20, 28, 50, 82) of protons or neutrons are characterized by large differences in separation energies of nucleons, which are similar to ionization energies of electrons and tend to be more stable.

One of the main goals for nuclear models is to accurately describe and predict the allowed energy levels of nuclei as well as interpret these levels. Using the shell model, which assumes a spherical nucleus, one can begin with assuming a nucleon is residing in a finite square well potential, which accounts for the fact that nucleons are well-bound within the nucleus and that nucleon density is relatively constant throughout the nucleus. However, this potential is unable to describe the magic numbers of nucleons by itself. The spin-orbit interaction must be included with the square well potential to account for these magic numbers. This is the interaction between the spin,  $s$ , and the orbital angular momentum,  $l$ , of the nucleons. Within this formalism, the energy levels of nucleons are labeled by the total angular momentum,  $j$ , which is the vector sum of  $s$  and  $l$ . The intrinsic spin of nucleons can either be  $\frac{1}{2}$  or  $-\frac{1}{2}$ , and experiments show that  $j=l-\frac{1}{2}$  shells are higher in energy than  $j=l+\frac{1}{2}$ . By including the spin-orbit term in the shell model, the magic numbers can be recreated where large energy gaps are predicted in levels containing the 2<sup>nd</sup>, 8<sup>th</sup>, 20<sup>th</sup>, 28<sup>th</sup>, 50<sup>th</sup>, and 82<sup>nd</sup> proton and/or neutron. The shell model can now be used to interpret the spins of states in a spherical nucleus.

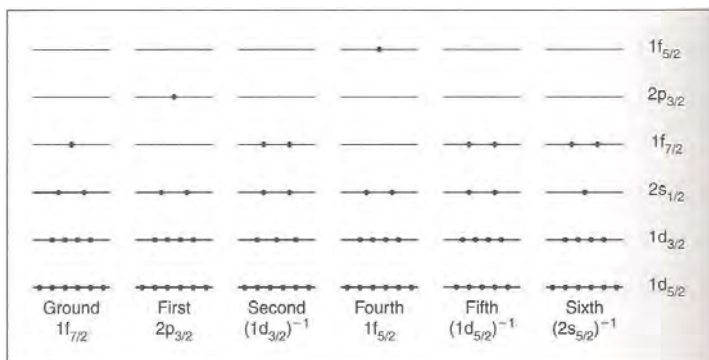
One must also consider the pairing of nucleons in time-reversed orbits to fully understand the nature of the energy levels. Proton-proton and neutron-neutron pairs are composed of nucleons with opposite  $j$  values. In other words, they are orbiting in opposite directions such that the total angular momentum of the pair sums to zero, as seen in Figure 3.3.



**Figure 3.3: Time reversed orbits of two nucleons with opposite  $j$ , first heading towards each other, then away from each other following a collision. [HAR 98]**

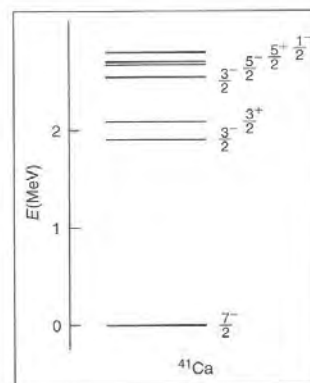
For all nuclei composed of both even numbers of protons and neutrons (even-even nuclei), the total nuclear spin,  $J$ , of the ground state (the lowest energy level in the nucleus) is equal to 0 because of this pairing. For odd-even or even-odd nuclei, the properties of the unpaired nucleons will determine the  $J$  of the ground state, as well as several of the low-energy excited states.

In much the same way that electrons can be promoted to higher energy levels to form excited states, so can nucleons. Excited states occur when nucleons occupy higher energy levels, but it should be noted these excited states are unstable and will eventually decay to the ground-state. For example, Figure 3.4a shows several neutron configurations for  $^{41}\text{Ca}$ . The far left neutron configuration is the ground state configuration; the unpaired neutron is in the  $1f_{7/2}$  orbital and has a spin and parity of  $7/2^-$ , which can be seen in Figure 3.4b. For the first excited state, the  $1f_{7/2}$  neutron is promoted to the  $2p_{3/2}$  orbital, resulting in a spin and parity of  $3/2^-$ . For the second excited state, a neutron is promoted from the  $1d_{3/2}$  orbital to the  $1f_{7/2}$  orbital, leaving an unpaired



**3.4a)**

**Figure 3.4a: Labeling scheme based on shell model for  $^{41}\text{Ca}$  in order to interpret the observed excited states for this nucleus for this nucleus shown in Figure 3.4b. [DUN 04]**



### 3.4b)

The shell model is suitable for spherical nuclei; however, if the nucleus is axially deformed (non-spherical), the shell model cannot accurately describe its features. The shell model must be modified by deforming the potential. In the 1950's, Sven Nilsson devised the Deformed Shell Model, which is suitable for axially deformed nuclei [NIL 55, NIL 69]. Assuming the nucleons move in a harmonic potential well and this well is axially symmetric along the z-axis, Nilsson solved the equation for the deformed harmonic oscillator in terms of  $\epsilon_2$ , the nuclear deformation parameter, and came up with diagrams for both protons and neutrons describing the energy of each orbital as a function of the deformation. A portion of the Nilsson proton diagram is shown in Figure 3.5. For  $^{171}\text{Re}$  at a deformation of  $\epsilon_2 = +0.22$ , the Fermi surface\* is predicted to lie in the  $9/2[514]$  level (circled in red), which originates from the  $h_{11/2}$  shell.

\* The Fermi surface is defined as the level in which the last unpaired nucleon resides.

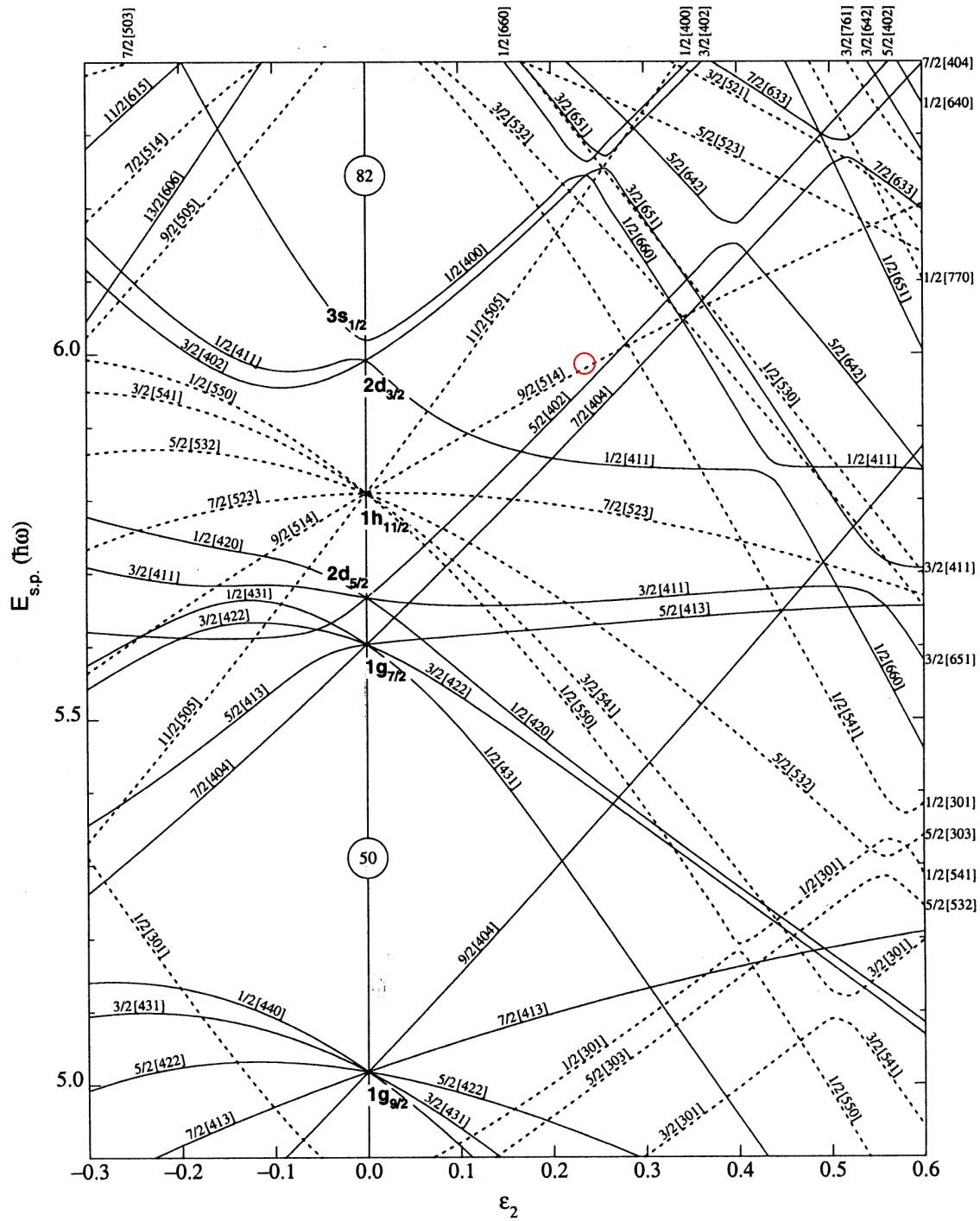
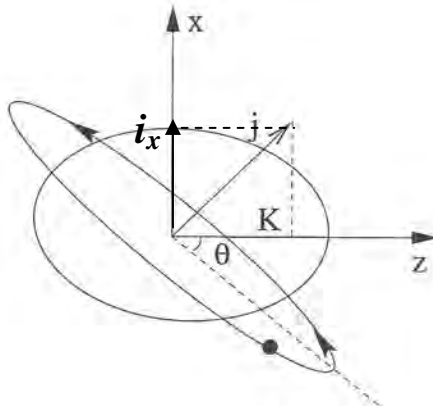


Figure 3.5: A portion of the Nilsson proton diagram. The Fermi surface for  $^{171}\text{Re}$  at a deformation of  $\epsilon_2 = +0.22$  is circled in red.



Nuclear deformation can either be negative, in which case the nucleus looks like a doorknob (oblate), or positive, where the nucleus looks like a football; this is called prolate deformation. If  $\epsilon_2=0$ , the nucleus is spherical, and the nucleons in one shell are degenerate, meaning that  $2j + 1$  nucleons that occupy that shell have the same energy. However, if  $\epsilon_2 \neq 0$ , each shell splits into orbitals of differing energies which are doubly degenerate. The orbitals have a complex labeling convention of  $K[Nn_z\Lambda]$ , where  $N$  is the principal quantum number of the shell before splitting,  $n_z$  is the number of nodes the wavefunction has along the  $z$ -axis, and  $\Lambda$  is the component of orbital angular momentum along the  $z$ -axis. The splitting is based on the value of  $K$  ( $K = 1/2, 3/2 \dots j$ ), which is a projection of  $j$  on the  $z$ -axis. The relationship between  $K$  and  $j$  can be seen in Figure 3.6. The lower values of  $K$  are energetically lower for prolate shapes as these represent orbitals where the nucleons lie closest to the rest of the nuclear matter. Each orbital holds two nucleons, corresponding to the pairing mentioned above, as the two nucleons traveling in opposite directions will have the same energy. This model can then be used in a similar fashion to the shell model to interpret ground and excited states. Using the Fermi surface for  $^{171}\text{Re}$  at a deformation of  $\epsilon_2 = +0.22$ , nearby levels include the  $5/2[402]$ ,  $1/2[541]$ ,  $1/2[411]$ , and  $1/2[660]$  levels.



**Figure 3.6: The relationship between  $j$  and  $K$ , where  $K$  is the component of  $j$  that lies along the symmetry axis. [HAR 98]**

Excited or high-spin states in prolate nuclei can be generated by rotating the nucleus.

Assuming the nucleus acts as a rigid body, the excited states follow the general equation

$$E_x = J(J+1)\frac{\hbar^2}{2\ell}$$

where  $\ell$  is the moment of inertia and  $J$  is the spin of the state. In returning

to the ground state, these nuclei will form decay sequences (rotational bands), which are built on each unpaired nucleon in an odd-A nucleus (a nucleus with an odd number of nucleons).

#### **D. Cranked Shell Model**

The deformed shell model is limited in its ability to explain nuclear structure because the model is based on a nucleus that is in its ground state. When the nucleus is in excited states, another model must be used to describe the effect of the rotation of the nucleus. The cranked shell model [BEN 79] expands on the deformed shell model and gives information on excited states in nuclei caused by nuclear rotation. As the entire nucleus is rotating, it exerts a force, called the Coriolis force, on the nucleons in time-reversed orbits. This Coriolis force acts in the same way as the one experienced as the earth rotates about its axis. The angular rotation of the nucleus as a whole induces individual nucleons to align their spins with the same axis as the nuclear rotation. This breaks the time-reversed orbits (and the final degeneracy). This is called a band crossing (also called a backbend), which will be discussed in more detail later. The Coriolis force is dependent not only on nuclear rotation but also the orbital the nucleon is residing in. The Coriolis force is proportional to  $j$ , so high- $j$  orbitals (such as the  $i_{13/2}$ ) tend to be affected more. A further discussion of the cranked shell model is beyond the scope of this project, but the model was used to predict where band crossings occur and will be discussed below.

To summarize, the shell model is relevant for spherical nuclei (nuclei that have a magic number of nucleons). The deformed shell model describes nuclei that do not have a magic number of nucleons and thus have some axial deformation. Both of these models describe nuclei in their ground states, but rotational states in excited nuclei are described by the cranked shell model.

### **E. Bands**

Figure 3.7 shows the level scheme for  $^{171}\text{Re}$  published in [CAR 93]. Part of the present experiment was confirming the previous results; new bands were found and existing bands were mapped to higher spins. All bands in the previous level scheme were labeled with the same convention as the current level scheme, shown in Figure 3.8, to make comparisons easier. There are several transitions linking individual bands to each other; however, no linking transitions have been seen connecting Band 5 to the rest of the structure. Due to this, it is uncertain whether Band 1 or Band 5 is the ground state.

USNA-1531-2

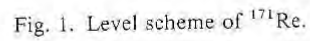
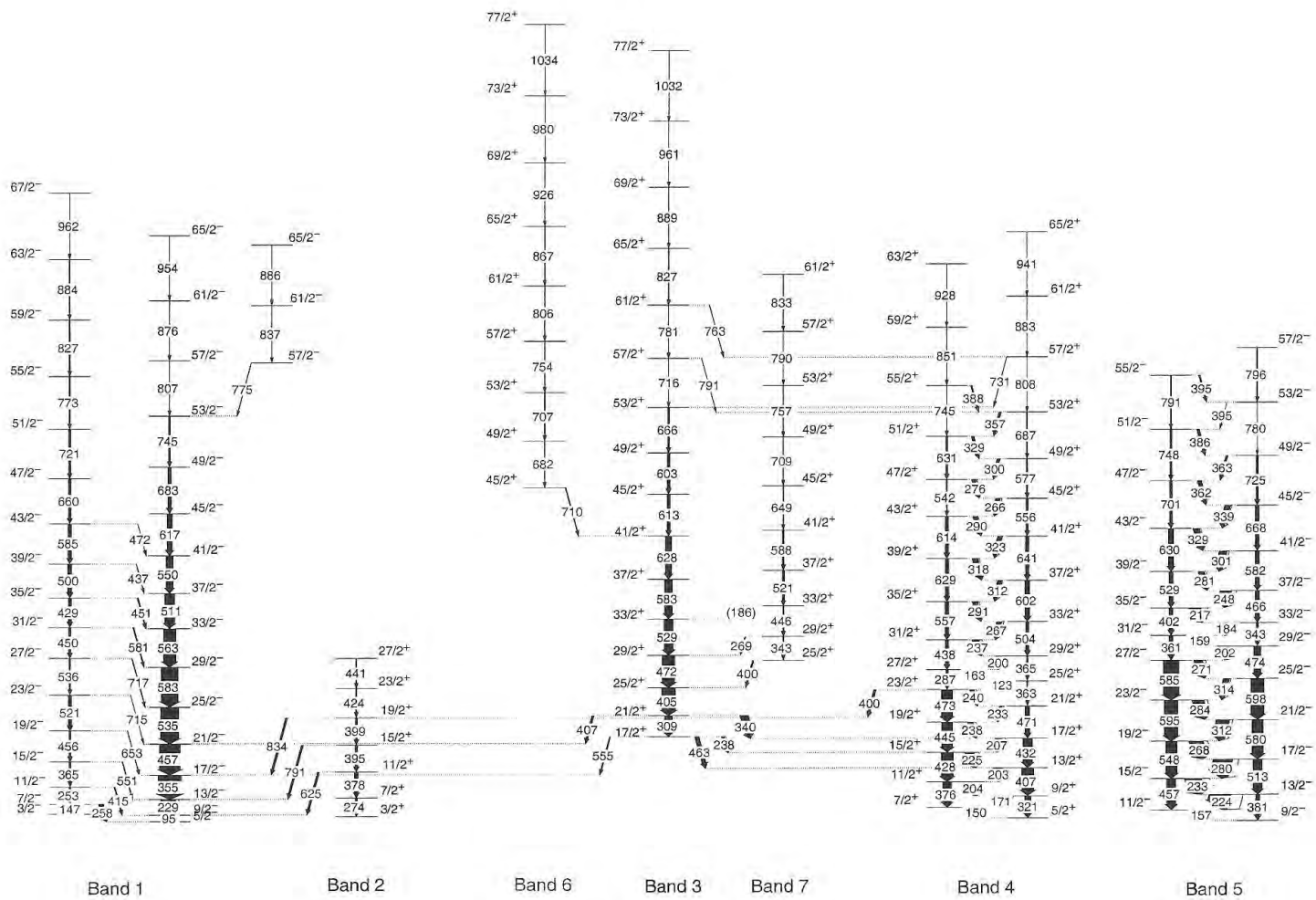


Figure 3.8: The level scheme for  $^{171}\text{Re}$  constructed in this experiment.



There are three basic types of bands. Some bands are strongly coupled, such as Bands 4 and 5 in Figure 3.8. These bands have two parallel E2 decay sequences that feed into each other via M1 transitions. Another type of band can be classified as decoupled, such as Band 3 in Figure 3.8. This band is just a single E2 sequence. Finally, there are weakly coupled bands, like Band 1 in Figure 3.8, where one E2 sequence feeds into the other.

Band 1: Band 1, which can be seen in Figure 3.8, was previously observed up to spin  $53/2^-$  and was extended up to spin  $65/2^-$  (three additional E2 transitions). Additionally, another transition (775 keV) was seen feeding into the  $53/2^-$  level. Two additional E2 transitions were seen above this transition. Previous results show a band (labeled Band 1a) feeding into Band 1 at  $25/2^-$  (with an energy of 451 keV) and  $27/2^-$  (297 keV). The recently collected data shows these linking transitions are incorrect, although Band 1a does feed Band 1. This band was extended from spin  $31/2^-$  down to spin  $3/2^-$  (seven new transitions were seen below what was previously known) and extended up an additional three transitions to  $67/2^-$ . Note there are several doublets (two  $\gamma$  rays of the same energy in the same event) in these bands. Without a coincidence cube, it would have been impossible to understand this band and likely led to the misinterpretation of [CAR 93]. Additionally, ten linking transitions between this band and Band 1 were seen. Three of these transitions (258 keV, 415 keV, and 717 keV) were strong enough to perform angular correlation ratios and were found to be M1 transitions. The ratios were found to be 0.906(18), 0.842(15), and 0.460(12) respectively.

Band 2: Band 2 can be seen in Figure 3.8 and was confirmed up to spin  $19/2^+$ . Above this, a 400 keV transition was previously placed in the band, but this transition was found to be a linking transition from the  $23/2^+$  state in Band 4 into the  $19/2^+$  state of Band 2. Finding this linking transition enabled the determination of the correct energy of the lowest state in the band, which differs from the reported value in [CAR 93]. The lowest state was originally assumed to be 388 keV but is now known to be at 68 keV. Three new transitions were seen feeding out of Band 2, from the  $19/2^+$ ,  $15/2^+$ , and  $11/2^+$  levels, into Band 1 at the  $17/2^-$ ,  $13/2^-$  and the  $9/2^-$  levels. These linking transitions were too weak to perform angular correlation ratios but they were assumed to be E1 transitions based on the configuration of Band 2 (see below).

Band 3: Band 3 can be seen in Figure 3.8 and was previously found up to spin  $53/2^+$ . An additional six transitions were added, taking the band up to spin  $77/2^+$ . Three linking transitions were seen feeding into band 4. Two of these transitions (463 keV and 340 keV) were found to be E2 transitions by angular correlation ratios of 1.415(31) and 1.223(14) respectively. This led to the confident assignment of a spin of  $17/2^+$  for the lowest state in the band, which is in agreement with previous data. Also, the  $57/2^+$  states of bands 3 and 5 were within 18 keV of each other. This led to mixing of their wavefunctions, which resulted in the linking transitions found between the bands, although these transitions were too weak to perform angular correlation ratios. Additionally, two new transitions were seen feeding Band 1. A 407 keV transition linked the  $21/2^+$  state in Band 3 with the  $21/2^-$  state in Band 1 and a 555 keV transition linked the  $17/2^+$  state in Band 3 with the  $17/2^-$  state in Band 1. These linking transitions were too

weak to perform angular correlation analyses. A spectrum of Band 3 can be seen in Figure 3.10a.

Band 4: Band 4 is a strongly coupled band. Band 4 was confirmed up to the  $51/2^+$  and  $53/2^+$  levels. Above that, new transitions were seen that are not in agreement with the previous data. The bands were extended up to  $63/2^+$  and  $65/2^+$  and several transitions were seen between Band 3 and Band 4 (previously discussed).

Band 5: Band 5 is also a strongly coupled band and was confirmed from the previous data. No additional transitions were seen building on this sequence, and no transitions were seen between this sequence and other sequences seen in  $^{171}\text{Re}$ . Spectra of Bands 4 and 5 can be seen in Figure 3.9.



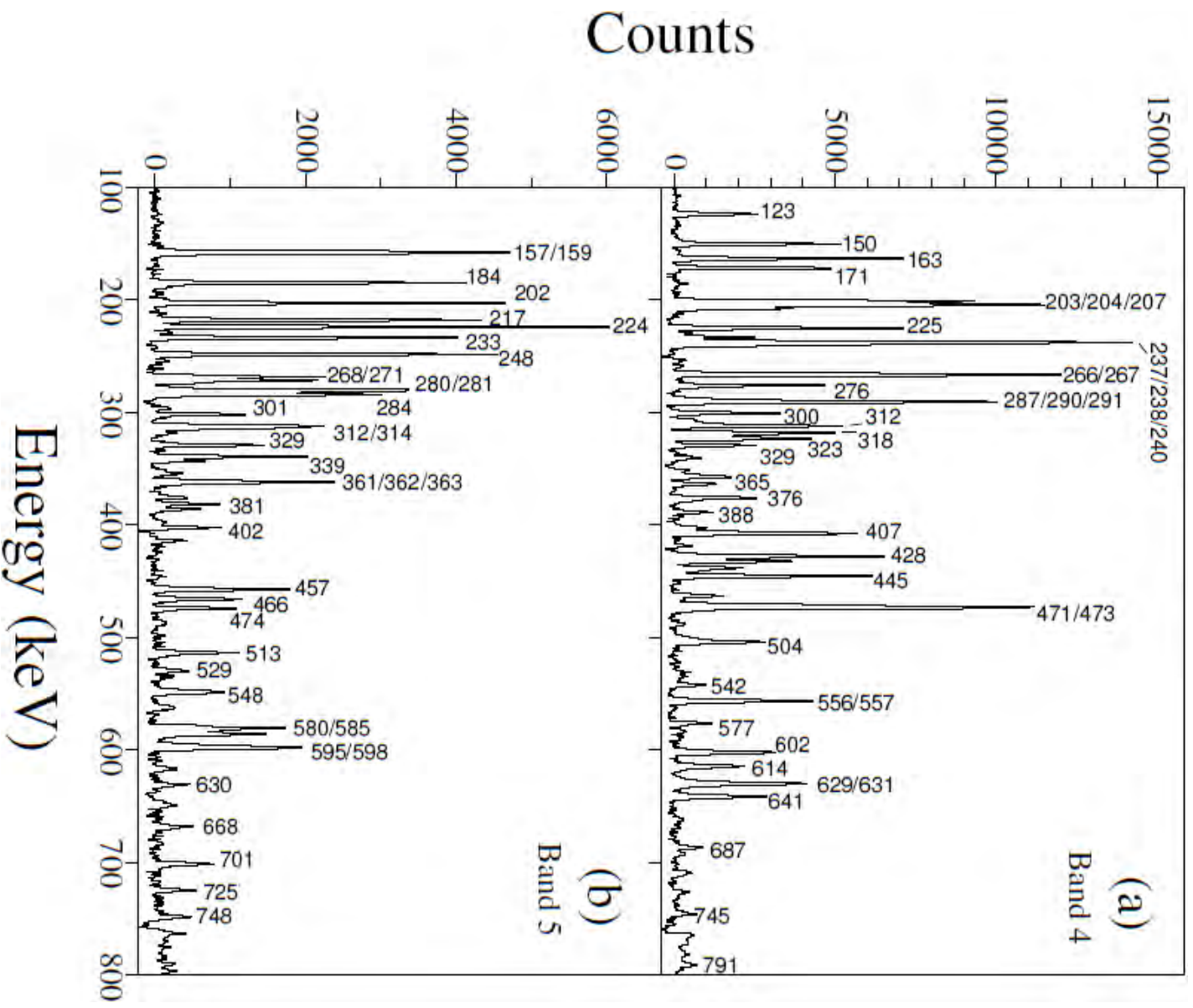


Figure 3.9:  $\gamma$  rays in Bands 4 and 5. These spectra were obtained by adding together multiple gates.

Bands 6 and 7: Bands 6 and 7 are both newly discovered bands that feed into Band 3 and are potential wobbling bands. Only one linking transition was found between Band 6 and Band 3 at  $41/2^+$  (710 keV); the linking transition was previously seen [CAR 93] and seven transitions were seen in the band, which was constructed up to spin  $73/2^+$ . The linking transition was too weak to perform an angular correlation analysis, so it has been assumed the linking transition is E2 in nature. Three transitions were seen linking Band 7 with Band 3 at  $25/2^+$  (400 keV),  $29/2^+$  (269 keV), and  $33/2^+$  (186 keV). These transitions were also too weak to perform angular correlation ratios and have been assumed to have no spin change, based on the energy of the other  $25/2$  levels in the level scheme. Nine transitions were seen in Band 7, and this sequence was seen up to spin  $61/2^+$ . Spectra of these bands can be seen in Figure 3.10. These bands will be analyzed further in future sections to determine if they are wobbling bands.

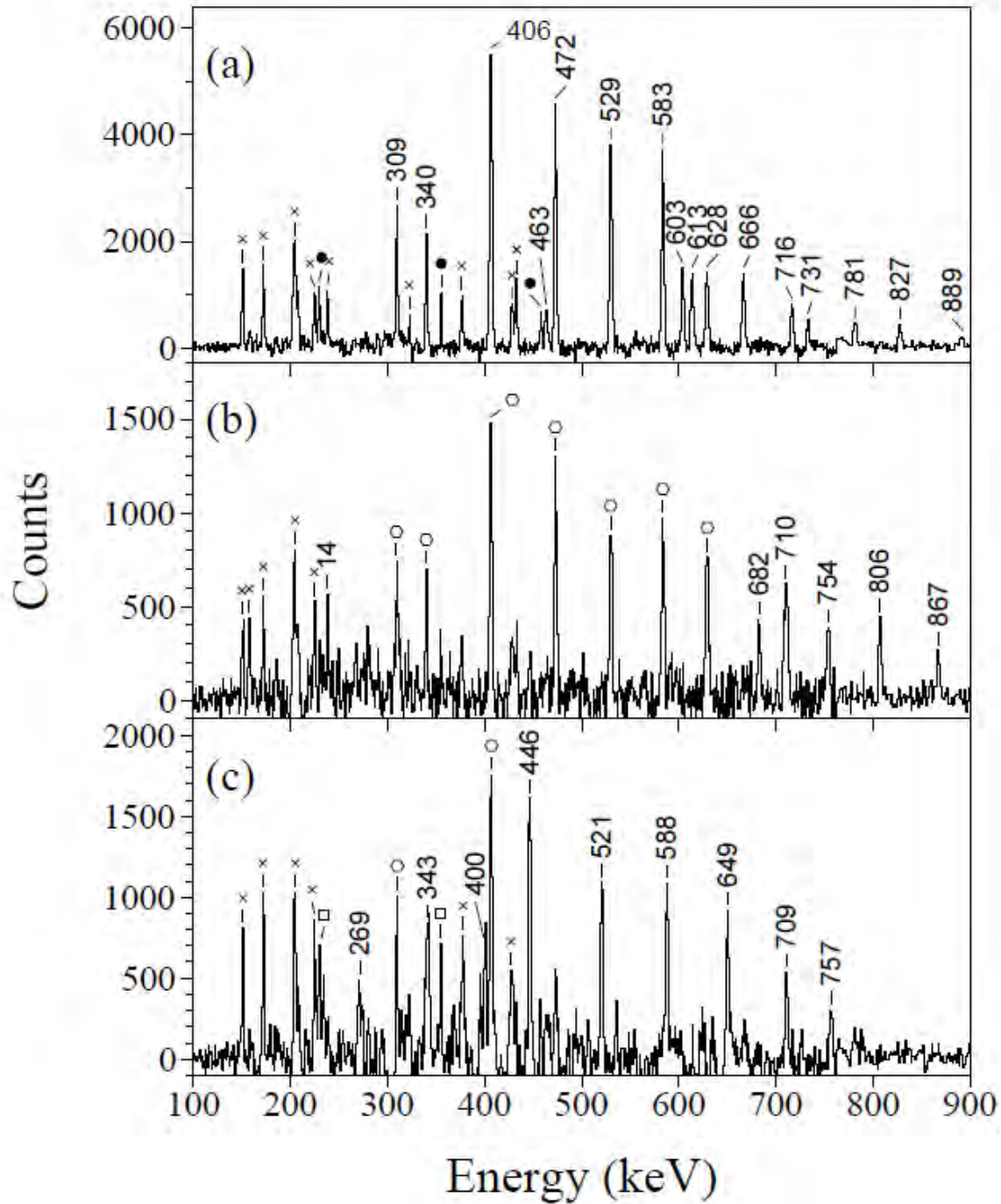


Figure 3.10:  $\gamma$  rays for Band 3 (3.10a), Band 6 (3.10b), and Band 7 (3.10c). These spectra were obtained by taking multiple gates. Other bands seen in the spectra are represented by x's (Band 4), closed circles (Band 1) and open hexagons (Band 3).

#### 4. Configurations

Each decay sequence in the level scheme of Figure 3.8 is based on the nucleus having a different configuration. In odd-Z, even-N nuclei, these different configurations generally arise from different unpaired protons in the nucleus. These unique decay sequences must now be correctly assigned to the configuration that stems from a particular unpaired proton. Referring back to the Nilsson diagram (Figure 3.5), the Fermi surface is predicted to lie on the  $9/2[514]$  orbital from the  $h_{11/2}$  shell. Nearby configurations include the  $5/2[402]$  orbital from the  $d_{5/2}$  shell, the  $1/2[411]$  from the  $d_{3/2}$  shell, the  $1/2[541]$  from the  $h_{9/2}$  shell, and the  $1/2[660]$  from the  $i_{13/2}$  shell. It is these configurations that are expected to be seen in the level scheme of  $^{171}\text{Re}$ . In order to match each band with a configuration, certain characteristics will be analyzed. These characteristics include whether the band is strongly coupled, weakly coupled, or decoupled, the initial alignment of the band, and the rotational frequencies of the band crossings, all of which will be described below. Table 4.1 summarizes the expected characteristics from the orbitals of interest as well as the assigned configurations for the bands.

Orbital	$i_x$ Expected (h)	Type of Band	Assignment
9/2[514]	1	Strongly Coupled	Band 5
5/2[402]	0	Strongly Coupled	Band 4
1/2[541]	3-4	Weakly Coupled	Band 1
1/2[411]	0	Decoupled	Band 2
$d_{3/2}$ (AB)	10	Decoupled	Band 7
1/2[660]	6	Decoupled	Band 3

**Table 4.1: A summary of each of the orbitals expected in the level scheme of  $^{171}\text{Re}$ , along with the expected initial alignment and the type of band structure for each orbital. The band assignment is in the far right column.**

As previously mentioned, there are three types of bands: strongly coupled, weakly coupled, and decoupled. Strongly-coupled bands are structures which have a high K value (recall that K is the projection of the angular momentum,  $j$ , along the symmetry axis). On the other hand, decoupled or weakly coupled bands are those which have a low K value. Those bands which are  $K = 1/2$  (and only  $K = 1/2$ ) have a decoupling constant in their wavefunction. This decoupling constant lowers the energy of the favored signature\* and raises the energy of the unfavored signature band, leading to a decoupled structure. The favored signature is determined by the equation  $\alpha_f = \frac{1}{2}(-1)^{j-1/2}$ . For example, the  $K = 9/2$  state from the  $h_{11/2}$  shell has  $\alpha_f = \frac{1}{2}(-1)^{11/2-1/2} = -1/2$ , which means the negative signature partner will be favored. Orbitals with the same parity and near a  $K = 1/2$  orbital will have some mixing in their wavefunctions from the  $K = 1/2$  state. This mixing will introduce some of the energy differentiation into the

---

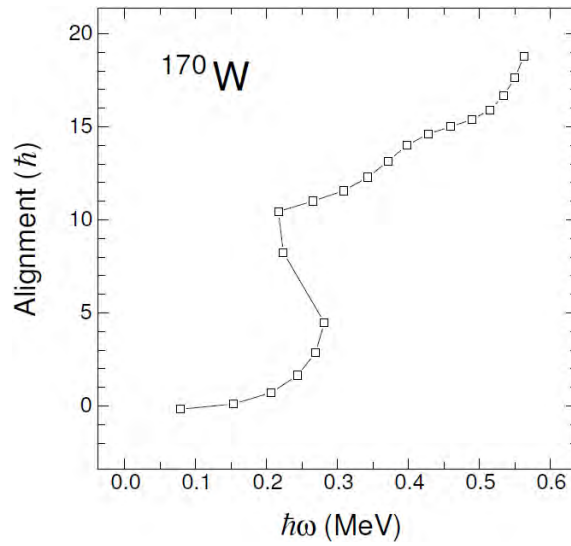
\* The signature ( $\alpha$ ) is associated with a  $180^\circ$  rotation around a principal axis. Nuclei with an odd number of nucleons can only have two signature values:  $+1/2$  and  $-1/2$ . Bands that have a positive signature  $\alpha = +1/2$  have spin states of  $1/2, 5/2, 9/2, \dots$ . Bands that have a negative signature  $\alpha = -1/2$  have spin states of  $3/2, 7/2, 11/2, \dots$ .

signatures, either decoupling them or causing them to be weakly coupled. High-K states, on the other hand, have very little mixing with the  $K = 1/2$  state because they are located far away from such an orbital. For example, looking at the Nilsson diagram (Figure 3.5), the  $5/2[402]$  orbital from the  $d_{5/2}$  shell is far from the  $K = 1/2$  orbital of the same shell ( $1/2[420]$ ), so there will be little mixing between these two wavefunctions. Thus, high-K states which do not experience this decoupling phenomenon are strongly coupled, with both signatures lying at similar energies.

It is therefore expected that Bands 4 and 5 are based on high-K states because they are strongly coupled and will likely be associated with either the  $9/2[514]$  orbital or the  $5/2[402]$  orbital. The other bands are based on lower-K states because they are weakly coupled or decoupled. These bands will likely be associated with the  $1/2[411]$ , the  $1/2[541]$ , or the  $1/2[660]$  orbitals.

As stated previously, the alignment of a band can also be used to help identify its configuration. Alignment is defined as the angular momentum of the unpaired particle projected onto the rotation axis, which is defined as the x-axis. This is displayed graphically in Figure 3.6, where one can see that if K is large, the alignment,  $i_x$ , will be small and vice versa. Therefore, nucleons with a high-K value will not have much initial alignment while nucleons with a low-K value are expected to have much more initial alignment. Alignment may be derived from the equation  $i_x(\omega) = I_x(\omega) - I_x^{ref}(\omega)$ , where  $I_x(\omega)$  is the total x-component of the angular momentum that is determined from the spins of the states, J, as well as the K value, and is defined by the equation  $I_x(\omega) = \sqrt{(J + 1/2)^2 - K^2}$ .  $I_x^{ref}(\omega)$  is the total x-component of the angular momentum of a reference configuration, which normally models the ground-state band of the even-even nucleus with one fewer nucleon than the nucleus of interest. This is because even-even nuclei

have no net alignment when they are in their ground state due to the time-reversed orbits of the nucleons always summing to zero angular momentum. In this case, the reference nucleus is  $^{170}\text{W}$ . The reference angular momentum is defined as  $I_x^{ref}(\omega) = \omega J_0 + \omega^3 J_1$ , where  $J_0$  and  $J_1$  are constants called the Harris parameters [HAR 65]. These constants were adjusted until the ground state reference band has no initial alignment at low frequency, as seen in Figure 4.1. The optimum Harris parameters were determined to be  $J_0 = 21 \hbar^2/\text{MeV}$  and  $J_1 = 50 \hbar^4/(\text{MeV})^3$ .



**Figure 4.1:** The alignment plot for  $^{170}\text{W}$  that was used to fit the Harris parameters, which were  $J_0 = 21 \hbar^2/\text{MeV}$  and  $J_1 = 50 \hbar^4/(\text{MeV})^3$ .

Using the definition of alignment with this reference, these values for each band are plotted in Figure 4.2 versus rotational energy ( $\hbar\omega \approx E_\gamma/2$ ).

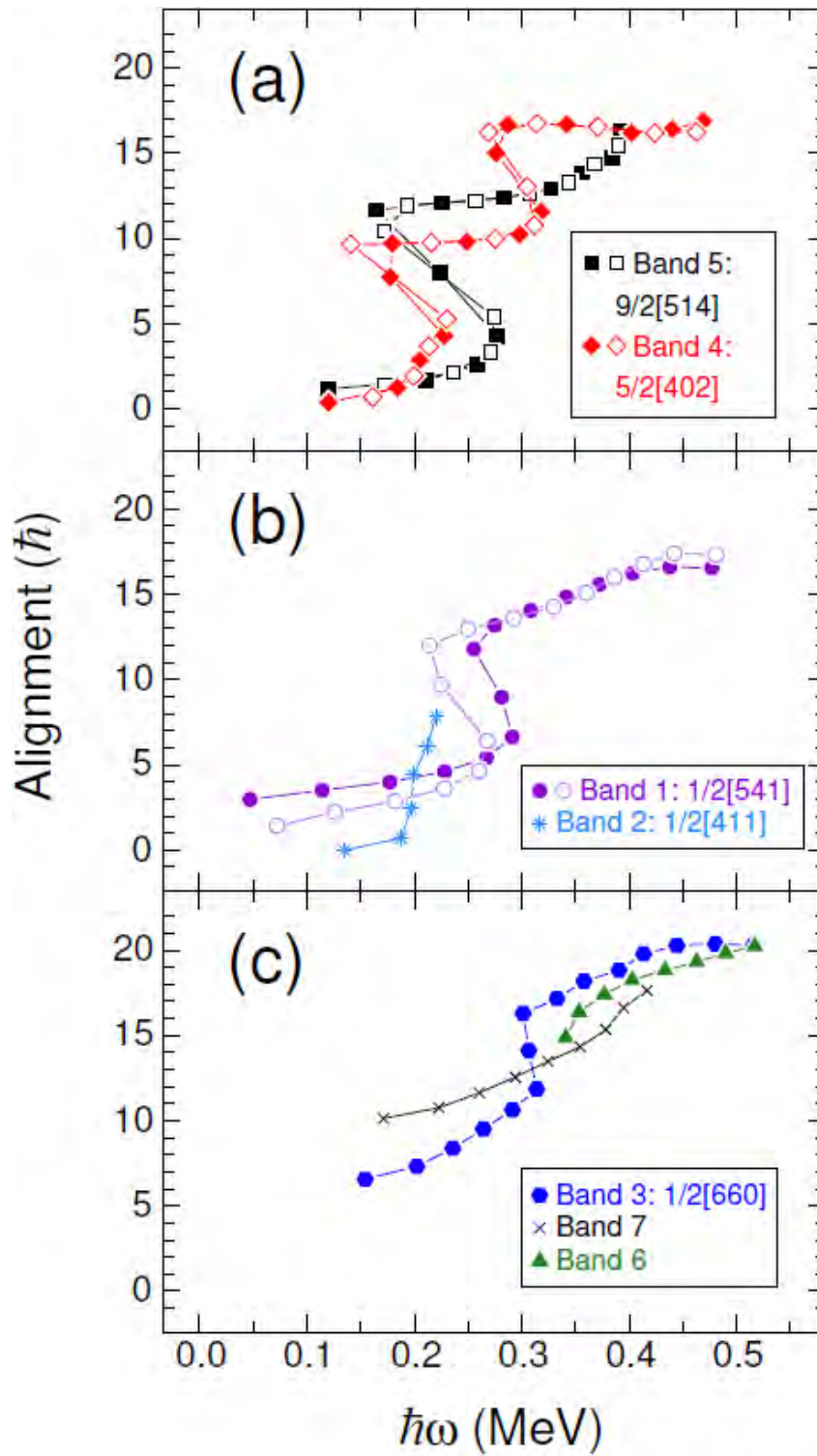


Figure 4.2: Alignment plots as a function of rotational energy ( $\hbar\omega$ ) for all 7 bands seen in  $^{171}\text{Re}$ .



Bands 4 and 5, the two strongly-coupled bands, were assigned configurations based on differences in their initial alignment, where  $\hbar\omega \approx 0.1$  MeV. Looking at the alignment plots for Bands 4 and 5, shown in Figure 4.2, it can be seen that Band 4 has slightly less initial alignment than Band 5; Band 4 has almost no initial alignment and Band 5 has about 1  $\hbar$  of initial alignment. The  $5/2[402]$  orbital comes from the  $d_{5/2}$  shell. This means that  $K = j$  and all the angular momentum is along the symmetry axis, so there is no initial alignment. This configuration matches the alignment plot for Band 4, and the  $5/2[402]$  configuration is assigned to this sequence. Looking at the  $9/2[514]$  orbital, which comes from the  $h_{11/2}$  shell, it is expected that because  $j = 11/2$  and  $K = 9/2$ , there will be a small amount of initial alignment (about 1  $\hbar$ ). This is consistent with the alignment plot of Band 5, and it is therefore assigned this configuration.

Band 3 has an initial alignment of about 6  $\hbar$ , which can be seen in Figure 4.2. This is the most initial alignment of any band in  $^{171}\text{Re}$ . Such a large initial alignment implies that it is from a low- $K$  state from a high- $j$  shell. Based on the Nilsson diagram (Figure 3.5), the  $1/2[660]$  orbital from the  $i_{13/2}$  shell is the only potential configuration ( $j = 13/2$ ) that can produce about 6  $\hbar$  of initial alignment. Thus, Band 3 is assigned the  $1/2[660]$  configuration.

Band 1 is a weakly-coupled band, with one signature partner appearing much stronger than the other. The stronger signature partner has about 3  $\hbar$  of initial alignment and the weaker signature partner has about 1  $\hbar$  of initial alignment. The amount of initial alignment present in the favored signature suggests that this configuration is also derived from a low- $K$  state of a high- $j$  shell but with a  $j$  less than the  $i_{13/2}$  orbital assigned to Band 3. The  $1/2[541]$  orbital from the  $h_{9/2}$  shell is expected to produce between 3 and 4  $\hbar$  of initial alignment. Based on these

arguments, the  $1/2[541]$  configuration is assigned to Band 1. In addition, for a weakly-coupled band, the unfavored signature characteristically has less alignment than its favored partner [JAN 01], which fits the profile of the unfavored partner in Band 1.

Band 2 has almost no initial alignment, meaning  $K$  and  $j$  must be similar, if not equal. However, the fact that only one signature is observed implies a low  $K$ . Only one configuration near the Fermi surface satisfies these characteristics, which is the  $1/2[411]$  orbital from the  $d_{3/2}$  shell. The  $1/2[411]$  orbital is expected to produce about  $1 \hbar$  of initial alignment. Thus, Band 2 is assigned this configuration.

Bands 6 and 7 cannot be associated with a single unpaired particle. Since they begin at such high energies and spins, they are likely based on multiple particles or perhaps a product of nuclear wobbling. Other characteristics such as band crossings must be used to assign a configuration to these bands.

Clearly, more nuclear structure information than just the initial alignment is revealed in the alignment plots of Figure 4.2. In some places, there are large gains in  $i_x$  while the rotational energy either remains nearly constant or actually decreases. This means the nucleus is gaining angular momentum without spinning faster, or in some cases, the nucleus is even slowing down. For example, looking at Figure 4.2, Band 1 gains large amounts of alignment near 0.3 MeV. These are called band crossings and result from the breaking of an individual pair of nucleons and the aligning of their angular momenta with that of the core of the nucleus. The rotating core of the nucleus exerts a Coriolis force on the pair of nucleons; this force acts in opposite directions on the pair, similar to how missiles fired in the northern and southern hemispheres are oppositely affected by the Coriolis force created by the rotation of the Earth. Nucleons in

orbitals with high- $j$  values are the most affected by this force. At some critical frequency, a pair of nucleons, for example the  $i_{13/2}$  neutrons, break from their time-reversed orbits and both neutrons align their angular momenta along the rotation axis. This imparts large amounts of angular momentum to the system without requiring the nucleus to spin faster.

The critical frequency at which this effect is observed is dependent on nuclear deformation. Different unpaired protons can drive the nucleus to different deformed shapes. The cranked shell model [BEN 79] can predict at what energy these band crossings will occur based on the deformation of the nucleus. The observed band crossing energies could be extracted from Figure 4.3, and then the cranked shell model calculations were run, where the amount of deformation was adjusted to reproduce the observed crossing frequencies. Figure 4.3 shows one such calculation from the cranked shell model. A deformation of  $\beta_2 = 0.333$  was input into the calculation. The details of the cranked shell model are beyond the scope of this project. The main point is that the solid black line and dotted red line represent the energies of the signature of the  $i_{13/2}$  neutron in the rotating frame. The predicted band crossing energy occurs at the inflection points found in Figure 4.3.

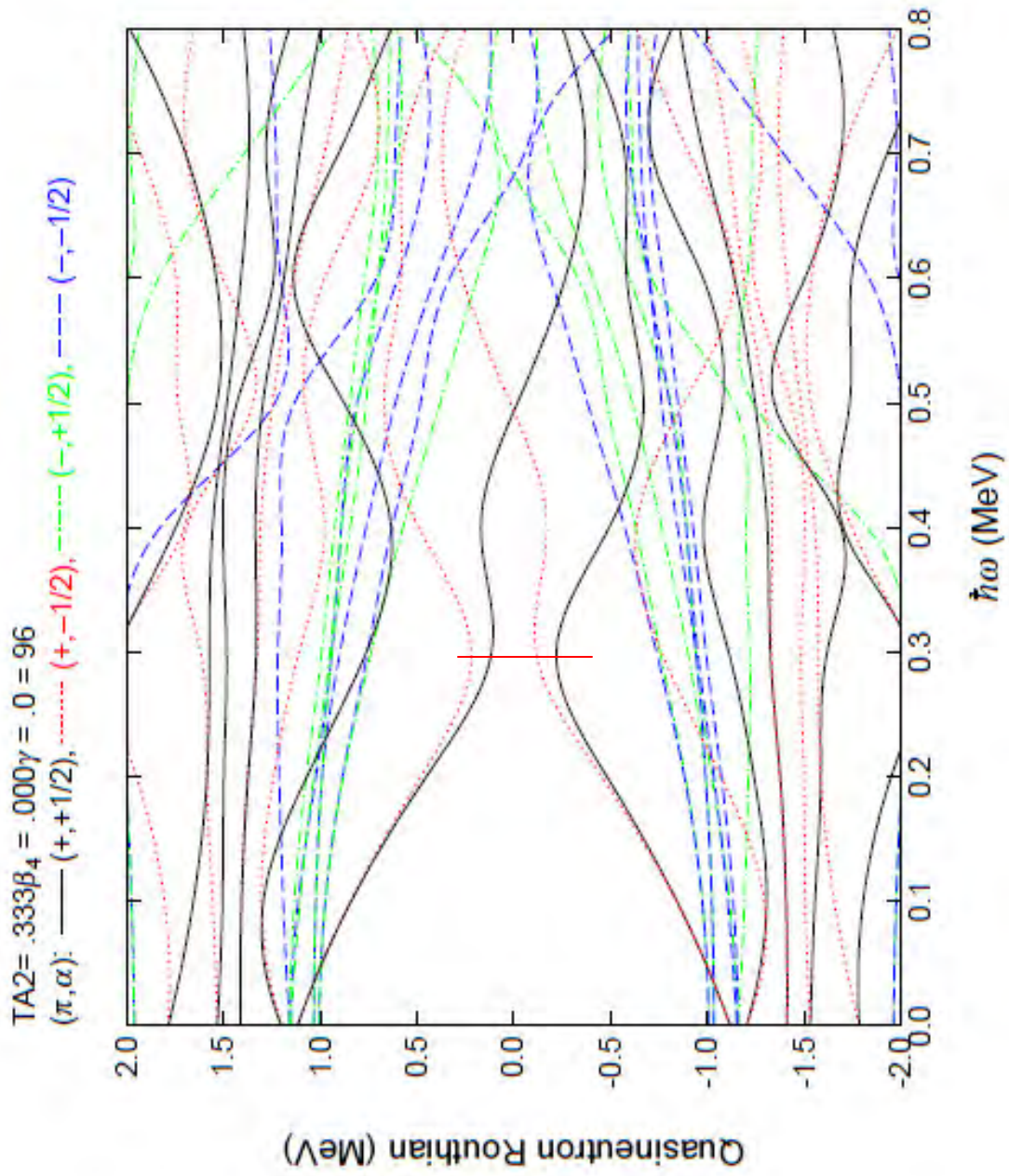


Figure 4.3: The cranked shell model calculations for a deformation of 0.333.

The red line in Figure 4.3 highlights where the calculated band crossing frequency would occur. In this instance, it occurs at 0.309 MeV, which is close to the observed band crossing frequency of 0.307 MeV for the  $i_{13/2}$  band. This process was used iteratively to determine the possible deformation for each band. Table 4.2 summarizes the observed band crossing energies and the determined deformation.

Band	Signature	Band Crossing (MeV)	$\beta_2$
$h_{9/2}$	+1/2	0.277	0.294
	-1/2	0.241	0.294
$i_{13/2}$	+1/2	0.307	0.333
$h_{11/2}$	+1/2	0.234	0.270
	-1/2	0.234	0.270
$d_{5/2}$	+1/2	0.202	0.210
	-1/2	0.200	0.210

**Table 4.2: Observed band crossings and subsequent determination of the deformation using the cranked shell model.**

It is interesting to note that the band crossings occur at different frequencies in the different bands. This means that different unpaired protons drive the nucleus to different amounts of deformation. That is, a single particle out of 171 changes the shape of the nucleus. Of the observed bands, the  $i_{13/2}$  band induces the greatest amount of deformation followed by the  $h_{9/2}$  band. The  $d_{5/2}$  band produces the least amount of deformation.

It is now possible to determine the likely configuration for Band 7, which is likely based on multiple particles. Looking at Figure 4.2, Band 7 begins with about 10  $\hbar$  of initial alignment, which is the amount of alignment that would come from the breaking the  $i_{13/2}$  neutrons from their time-reversed orbit, based on the fact that every other band gains about 10  $\hbar$  of alignment after the band crossing. This implies that the original proton brought in almost no alignment, meaning

it is from a low-K orbital. Looking at the alignment plots and configuration assignments for the other bands, Band 7 is assigned the  $1/2[411]$  configuration from the  $d_{3/2}$  shell, since it has nearly no alignment associated with it, but it is also decoupled. This is the same configuration as Band 2, and it is believed that Band 7 is the unfavored signature partner of Band 2. Band 6 will be discussed in the next section.

## 5. Wobbling Mode

The wobbling mode in high-spin nuclei is analogous to the spinning of an asymmetric top. In most rotational and symmetric nuclei, the spin generated by the nucleus lies along a single axis. However, if there is no symmetry of the mass distribution (that is, it has an asymmetric shape), the angular momentum may lie on any of the three principle axes and therefore the total angular momentum vector lies off axis, allowing for precession and wobbling about one of the principle axes. The result of this motion would be a separate decay sequence based on the proton of another sequence, but lying at higher energy. The wobbling band was first discovered in  $^{163}\text{Lu}$  [ØDE 01], where the unpaired  $i_{13/2}$  proton forces the nucleus to become more deformed in comparison with structures based on the other unpaired protons. When this occurs, a gap in the neutron energy levels, analogous to the magic numbers in the shell model, forms at  $N=94$ . In the level scheme of  $^{163}\text{Lu}$ , shown in Figure 5.1, the  $i_{13/2}$  band is labeled as TSD 1, which stands for triaxial (another name for asymmetric) strongly deformed. The wobbling band is based on the  $i_{13/2}$  band and is labeled as TSD 2 in Figure 5.1.

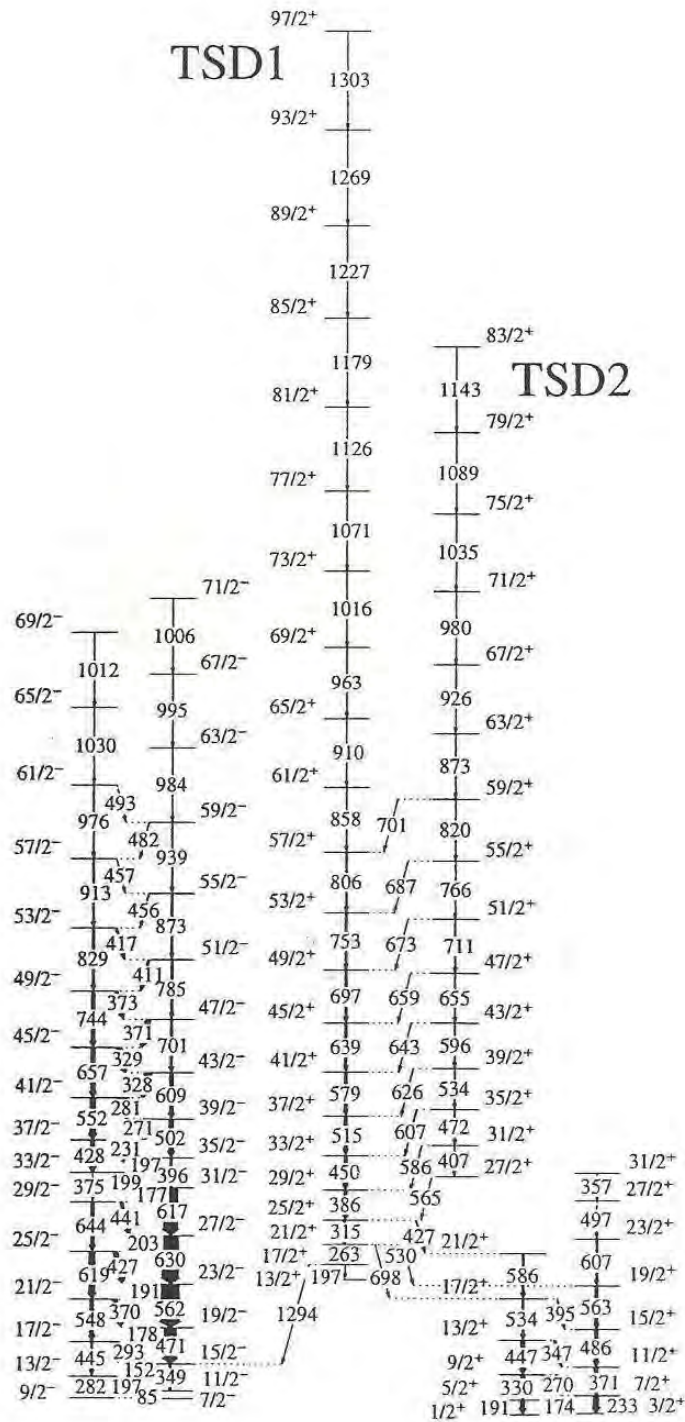
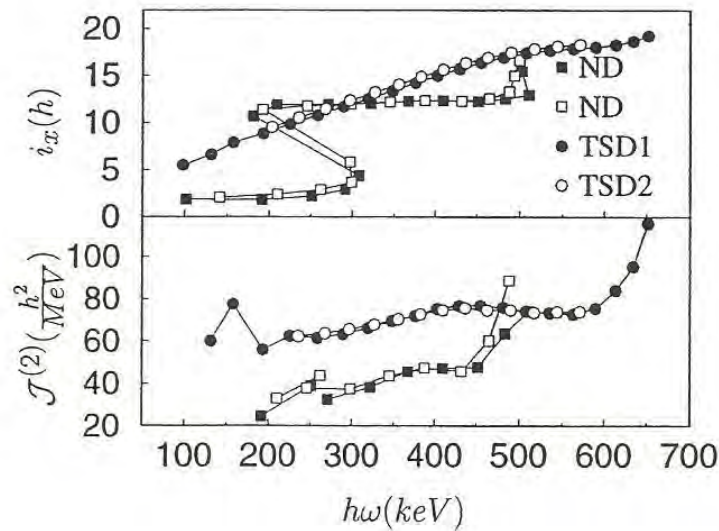


Figure 5.1: The level scheme of  $^{163}\text{Lu}$  showing the  $i_{13/2}$  band (TSD 1) and the wobbling structure (TSD 2). The arrows denote  $\gamma$ -ray transitions between states with their energy given in units of keV. [ØDE 01]



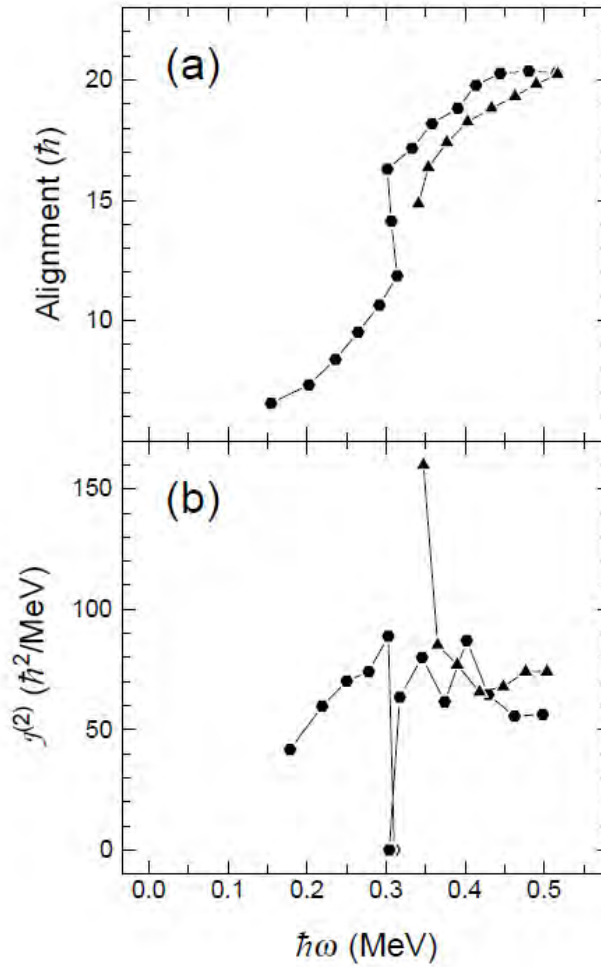
The characteristics of the wobbling band are unique. Both the wobbling band and the favored band are based on the  $i_{13/2}$  orbital; for the wobbling band, the total angular momentum vector  $J$  lies further off axis. Because these two bands are based on the same proton, characteristics such as alignment (the angular momentum from unpaired nucleons) and the dynamic moment of inertia (inversely proportional to the change in energy of sequential  $\gamma$  rays in a decay sequence) are the same. The dynamic moment of inertia is a very sensitive parameter and very rarely is it the same for different bands. As can be seen in Figure 5.2, plots of alignment ( $i_x$ ) and moment of inertia ( $J^{(2)}$ ) versus rotational frequency for  $^{163}\text{Lu}$  shows the  $i_{13/2}$  band (TSD 1) and the wobbling band (TSD 2) are nearly the same [ØDE 01]. This is the signal that was sought in  $^{171}\text{Re}$ .



**Figure 5.2: Top: Alignment versus rotational frequency, comparing the  $i_{13/2}$  band (TSD 1) and the wobbling band (TSD 2). Bottom: Dynamic moment of inertia versus rotational frequency. [ØDE 01]**

Figure 5.3, like Figure 5.2, shows the alignment and dynamic moment of inertia versus rotational frequency for the potential wobbling band and the  $i_{13/2}$  band of  $^{171}\text{Re}$ . The top panel,

which shows the alignment plots for Bands 3 ( $i_{13/2}$ ) and 6, shows that the alignment for Band 6 tracks the alignment of Band 3, but does not exactly match the values. Band 6 has about  $1\hbar$  less alignment at the start of the band and eventually reaches the same amount of alignment.



**Figure 5.3: a) Alignment for the  $i_{13/2}$  band and Band 6, the potential wobbling band. B) A comparison of the dynamic moment of inertia for the  $i_{13/2}$  band and Band 6. In both plots, the  $i_{13/2}$  band is depicted by circles and Band 6 is depicted by triangles.**

Looking at the bottom panel, it is clear that the dynamic moment of inertia also does not match up for Bands 3 and 6. The zig-zag in the dynamic moment of inertia for the  $i_{13/2}$  band at 0.40 MeV is a result of the interaction of this band with Band 4. Without this interaction, the dynamic moment of inertia for the  $i_{13/2}$  band above 0.35 MeV would be a more smooth curve, similar to the one observed in Band 6. Once again, these plots do not line up exactly, but because the plots track each other, Band 6 cannot definitively be completely ruled out as a wobbling band.

Another characteristic of wobbling bands is that there are many transitions linking the wobbling band to the  $i_{13/2}$  band. This can be seen in Figure 5.1 for  $^{163}\text{Lu}$ . For  $^{171}\text{Re}$ , only one linking transition was observed. This could be because there really only is one linking transition, or it could be due to the fact that data was collected for only sixteen hours. The transitions, if they exist, are very weak, and there may not be enough data to see them.

## 6. Conclusion and Future Work

After the experiment was performed in March 2010, the data was prepared by checking for gain shifts, calibrating the detectors, correcting for Doppler shifts, and sorting the data into the Blue database. The level scheme of  $^{171}\text{Re}$  was constructed from these data, building off the level scheme by [CAR 93]. Several bands were extended to higher spins, and two new bands were found feeding into the  $i_{13/2}$  sequence. Configurations were assigned for six of the seven bands, and Band 6 was analyzed to determine if it is a wobbling band.

Questions still remain as to whether  $^{171}\text{Re}$  has an asymmetric nucleus or not. The alignment and dynamic moment of inertia for Band 6 track that of the  $i_{13/2}$  band; however, they do not line up. In order to definitively determine whether or not this is the case, another experiment must be run on  $^{171}\text{Re}$  for several days in order to gather enough statistics. In this experiment, only 16 hours of data were collected on  $^{171}\text{Re}$ . With more data, some of the weaker sequences, including the potential wobbling band will be more strongly populated, and transitions that were too weak to be seen in this experiment might be seen in a later experiment.

## 7. Bibliography

AMR 03: H. Amro *et al.*, Physics Letters B **553**, 197 (2003).

BEN 79: R. Bengtsson and S. Frauendorf, Nuclear Physics **A314**, 27 (1979).

R. Bengtsson and S. Frauendorf, Nuclear Physics **A327**, 139 (1979).

BRI 06: P. Bringel *et al.*, Physical Review C **73**, 054314 (2006).

CAR 93: H. Carlsson *et al.*, Nuclear Physics **A551**, 2 (1993).

CRO 01: M. Cromaz *et al.*, *Nuclear Instrumentation and Methods A* **462**, 519 (2001).

DUN 04: R. A. Dunlap, *The Physics of Nuclei and Particles*, (Brooks/Cole: Belmont),  
2004.

ESP 94: J. Espino *et al.*, Nuclear Physics **A567**, 2 (1994).

HAR 65: S.M. Harris, Physical Review **138B**, 509 (1965).

HAR 98: D. J. Hartley, PhD Thesis, Florida State University (1998).

HAR 05a: D. J. Hartley *et al.*, Physical Review C **72**, 064325 (2005).

HAR 05b: D. J. Hartley *et al.*, Physics Letters B **608**, 31 (2005).

HAR 06: D. J. Hartley *et al.*, Physical Review C **74**, 054314 (2006).

HAR 09: D. J. Hartley *et al.*, Physical Review C **80**, 041304 (2009).

JAN 96: R.V.F. Janssens and F. S. Stephens, *Nuclear Physics News* **6**, 9 (1996).

JAN 01: H. J. Jansen *et al.*, Nuclear Physics **A695**, 3 (2001).

NIL 55: S.G. Nilsson, Dan. Mat. Fys. Medd. **29**, No. 16 (1955).

NIL 69: S.G. Nilsson, C.F. Tsang, A. Sobiczewski, Z. Szymanski, S. Wycech, C.

Gustafson, I.L. Lamm, P. Moller, and B. Nilsson, Nuclear Physics **A131**, 1 (1969).

ØDE 01: S. W. Ødegård *et al.*, Physical Review Letters **86**, 5866 (2001).

PAT 07: N. S. Pattabiramann *et al.*, Physics Letters B **647**, 243 (2007).

REC 85: J. Recht *et al.*, Nuclear Physics **A440**, 2 (1985).

SCH 03: G. Schwönwaßer *et al.*, Physics Letters B **552**, 9 (2003).

WAN 04: H.L. Wang *et al.*, Physical Review C **70**, 064306 (2004).

## Appendix 1: Definition of Terms

$\gamma$  ray: a form of electromagnetic radiation

MeV (and keV): megaelectron volts and kiloelectron volts. Units of energy

$E_\gamma$ : The energy of a  $\gamma$  ray

M1: Magnetic dipole transition

E1: Electric dipole transition

E2: Electric quadrupole transition

$\beta_2$ : nuclear quadrupole deformation; used in cranked shell model calculations

$n$ : principle quantum number

$l$ : the orbital angular momentum

$s$ : spin quantum number

$j$ : the total angular momentum, which is the vector sum of  $s$  and  $l$

$\epsilon_2$ : nuclear deformation

$K[Nn_z\Lambda]$

$K$ : the projection of  $j$  along the z-axis

$N$ : the principal quantum number of the shell

$n_z$ : the number of nodes the wavefunction has along the z-axis

$\Lambda$ : the component of orbital angular momentum along the z-axis

x-axis: the rotation axis

z-axis: the symmetry axis

$\ell$ : the moment of inertia

$N$ : the number of neutrons in a nucleus

$Z$ : the number of protons in a nucleus

$A$ : the total number of nucleons (protons and neutrons) in a nucleus

$\alpha$ : the signature ( $\alpha$ ) is associated with a  $180^\circ$  rotation around a principal axis.

$\alpha_f$ : the favored signature ( $\alpha_f$ ) is determined by the equation  $\alpha_f = \frac{1}{2}(-1)^j - 1/2$  and is often the more strongly populated sequence

$i_x(\omega)$ : the alignment,  $i_x(\omega)$ , is the angular momentum of the unpaired particle projected onto the rotation axis

$\hbar$ : units of angular momentum

Harris Parameters  $J_0$  and  $J_1$ : constants used to adjust the initial alignment of the reference nucleus to zero



## Appendix 2: Angular Correlation Ratios

### Band 1

Gates	511/550	682/535	745/535				
$E_\gamma$	Rings 6-10	Uncertainty	Rings 12-16	Uncertainty	Ratio	Uncertainty	Transition
229	2607	104	2870	108	1.101	0.06	E2
355	2917	110	3713	122	1.273	0.06	E2
457	2383	100	3078	114	1.292	0.07	E2
511	226	38	138	32	0.611	0.17	E2
535	2187	96	2879	110	1.316	0.08	E2
563	2112	96	3412	120	1.616	0.09	E2
583	2059	94	3125	114	1.518	0.09	E2
617	1383	78	2133	96	1.542	0.11	E2
683	738	60	1106	72	1.499	0.16	E2
745	460	50	690	58	1.500	0.21	E2
775	1661	36	265	40	0.160	0.02	E2
807	216	38	235	40	1.088	0.27	E2

### Band 1a

Gates	500/585	429/660	450/535	660/721			
$E_\gamma$	Rings 6-10	Uncertainty	Rings 12-16	Uncertainty	Ratio	Uncertainty	Transition
253	444	44	502	46	1.131	0.15	E2
258	267	36	242	34	0.906	0.18	M1
365	763	62	745	62	0.976	0.11	E2
415	411	50	346	46	0.842	0.15	M1
429	1877	92	2665	108	1.420	0.09	E2
450	1688	88	1625	86	0.963	0.07	M1
456	3250	118	4149	132	1.277	0.06	E2
500	1370	80	1920	94	1.401	0.11	E2
521	928	68	1351	80	1.456	0.14	E2
585	3301	120	4318	136	1.308	0.06	E2
660	1262	78	1637	88	1.297	0.11	E2
715	618	72	284	68	0.460	0.12	M1
721	1050	84	1533	100	1.460	0.15	E2
773	859	68	1382	82	1.609	0.16	E2
827	584	58	746	64	1.277	0.17	E2
884	395	52	587	60	1.486	0.25	E2

**Band 2**

Gates	400/424	400/441	377/400				
$E_\gamma$	Rings 6-10	Uncertainty	Rings 12-16	Uncertainty	Ratio	Uncertainty	Transition
274	2007	90	2347	98	1.169	0.07	E2
378	725	56	904	62	1.247	0.13	E2
395	2579	104	2965	112	1.150	0.06	E2
399	840	62	967	68	1.151	0.12	E2
424	927	62	1262	72	1.361	0.12	E2
441	492	46	645	52	1.311	0.16	E2

**Band 3**

Gates	603/613	628/583	530/603	666/472			
$E_\gamma$	Rings 6-10	Uncertainty	Rings 12-16	Uncertainty	Ratio	Uncertainty	Transition
238	221	32	114	24	0.516	0.13	M1
309	583	50	600	50	1.029	0.12	E2
340	618	52	756	56	1.223	0.14	E2
405	1731	112	2187	134	1.263	0.11	E2
407	122	78	217	94	1.779	1.37	***
463	200	34	283	38	1.415	0.31	E2
472	1131	70	1568	82	1.386	0.11	E2
529	910	64	1390	78	1.527	0.14	E2
583	654	56	1100	70	1.682	0.18	E2
603	528	50	262	38	0.496	0.09	E2
613	1054	68	1378	78	1.307	0.11	E2
628	1046	68	1615	84	1.544	0.13	E2
666	811	60	1116	70	1.376	0.13	E2
716	172	32	248	38	1.442	0.35	E2
781	120	30	143	32	1.192	0.40	E2
827	91	28	149	32	1.637	0.61	E2

**Band 4**

Gates	473/445	628/613	603/504	200/237			
$E_\gamma$	Rings 6-10	Uncertainty	Rings 12-16	Uncertainty	Ratio	Uncertainty	Transition
123	847	62	759	60	0.896	0.10	M1/E2
150	1649	84	1552	82	0.941	0.07	M1/E2
163	2218	98	2243	98	1.011	0.06	M1/E2
171	1799	88	1859	90	1.033	0.07	M1/E2
200	1210	88	1132	86	0.936	0.10	M1/E2
204	2795	120	280	120	0.100	0.04	M1/E2
225	1748	88	1752	88	1.002	0.07	M1/E2
237	2200	98	2223	98	1.010	0.06	M1/E2
266	2654	106	3064	114	1.154	0.06	M1/E2
276	780	62	771	60	0.988	0.11	M1/E2
287	437	56	503	60	1.151	0.20	M1/E2
290	2088	100	2144	102	1.027	0.07	M1/E2
300	570	54	630	56	1.105	0.14	M1/E2
312	1128	72	1280	76	1.135	0.10	M1/E2
318	1204	76	1153	74	0.958	0.09	M1/E2
323	1306	78	1344	80	1.029	0.09	M1/E2
329	491	50	500	52	1.018	0.15	M1/E2
340	439	48	543	52	1.237	0.18	M1/E2
357	492	50	429	48	0.872	0.13	M1/E2
376	1153	72	1209	74	1.049	0.09	E2
388	223	38	203	38	0.910	0.23	M1/E2
407	1671	86	1877	90	1.123	0.08	E2
428	1759	90	2055	96	1.168	0.08	E2
432	672	62	797	64	1.186	0.15	E2
445	658	58	922	66	1.401	0.16	E2
473	1977	94	2757	108	1.395	0.09	E2
504	415	48	623	56	1.501	0.22	E2
542	148	36	272	42	1.838	0.53	E2
557	894	66	1271	76	1.422	0.14	E2
577	186	38	155	42	0.833	0.28	E2
602	1069	72	1265	76	1.183	0.11	E2
614	431	50	507	52	1.176	0.18	E2
629	866	66	1338	78	1.545	0.15	E2
641	616	58	1020	70	1.656	0.19	E2
745	220	40	305	44	1.386	0.32	E2

**Band 5**

Gates	585/595	580/598	248/329	202/271			
$E_\gamma$	Rings 6-10	Uncertainty	Rings 12-16	Uncertainty	Ratio	Uncertainty	Transition
157	5952	156	5826	154	0.979	0.04	M1/E2
184	3786	124	3394	118	0.896	0.04	M1/E2
202	2079	94	1870	88	0.899	0.06	M1/E2
217	4388	134	4061	130	0.925	0.04	M1/E2
224	4316	132	4939	142	1.144	0.05	M1/E2
233	3484	120	3868	126	1.110	0.05	M1/E2
248	2817	108	2733	106	0.970	0.05	M1/E2
268	2062	104	1992	100	0.966	0.07	M1/E2
271	1762	98	1788	96	1.015	0.08	M1/E2
280	7278	172	7823	178	1.075	0.04	M1/E2
301	2238	96	2149	94	0.960	0.06	M1/E2
312	1437	176	1890	172	1.315	0.20	M1/E2
314	2018	182	1857	170	0.920	0.12	M1/E2
329	1594	82	1306	74	0.819	0.06	M1/E2
339	2191	96	2015	92	0.920	0.06	M1/E2
363	2367	100	2329	98	0.984	0.06	M1/E2
381	866	62	959	64	1.107	0.11	E2
457	1423	78	1633	84	1.148	0.09	E2
466	648	54	887	62	1.369	0.15	E2
474	607	52	817	60	1.346	0.15	E2
513	2235	98	2346	100	1.050	0.06	E2
529	449	48	698	58	1.555	0.21	E2
548	1623	84	2254	98	1.389	0.09	E2
580	1699	104	2476	122	1.457	0.11	E2
585	1410	98	2012	114	1.427	0.13	E2
595	1744	248	1892	332	1.085	0.25	E2
598	1378	246	1939	332	1.407	0.35	E2
630	427	48	791	62	1.852	0.25	E2
668	703	58	823	62	1.171	0.13	E2
701	785	62	1443	80	1.838	0.18	E2
725	615	56	925	66	1.504	0.17	E2
748	733	60	860	64	1.173	0.13	E2
796	436	50	490	52	1.124	0.18	E2